

Understanding the Mechanism and Importance of Brown Carbon Bleaching Across the Visible Spectrum in Biomass Burning Plumes from the WE-CAN Campaign

Yingjie Shen¹, Rudra P. Pokhrel^{1, a}, Amy P. Sullivan², Ezra J. T. Levin^{2, b}, Lauren A. Garofalo³, Delphine K. Farmer³, Wade Permar⁴, Lu Hu⁴, Darin W. Toohey⁵, Teresa Campos⁶, Emily V. Fischer², Shane M. Murphy¹

¹Department of Atmospheric Science, University of Wyoming, Laramie, WY 82071, USA.

²Department of Atmospheric Science, Colorado State University, Fort Collins, CO 80523, USA

³Department of Chemistry, Colorado State University, Fort Collins, CO 80523, USA

⁴Department of Chemistry and Biochemistry, University of Montana, Missoula, MT 59812, USA.

⁵Department of Atmospheric and Oceanic Sciences, University of Colorado Boulder, Boulder, CO 80309, USA

⁶National Center for Atmospheric Research, Atmospheric Chemistry Division, Boulder, CO 80301, USA

^anow at Air Pollution Control Division, Colorado Department of Public Health and Environment, Denver, CO 80246, USA

^bnow at METEC Research Group, Colorado State University Energy Institute, Fort Collins, CO 80524, USA

Corresponding author: Shane M. Murphy (shane.murphy@uwyo.edu)

Abstract. Aerosol absorption of visible light has an important impact on global radiative forcing. Wildfires are one of the major sources of light-absorbing aerosol, but there remains significant uncertainty about the magnitude, wavelength dependence, and bleaching of absorption from biomass burning aerosol. We collected and analyzed data from 21 Western United States wildfire smoke plumes during the 2018 WE-CAN airborne measurement campaign to determine the contribution of black carbon (BC), brown carbon (BrC), and lensing to the aerosol mass absorption cross-section (MAC). Comparison to commonly used parameterizations and modeling studies suggest model overestimation of absorption is likely due to incorrect BrC refractive indices. Modelers (Wang et al. 2018; Carter et al. 2021) invoke a bleaching process that decreases the MAC of organic aerosol (OA) to offset the overestimation of absorption in models. However, no evidence of decreasing MAC is observed in individual WE-CAN fire plumes or in aged plumes from multiple fires. A decrease in OA mass and water-soluble organic carbon (WSOC), both normalized by CO to correct for dilution, is observed with increasing oxygen to carbon (O:C) ratio and decreasing gas-phase toluene:benzene ratio, when data from all fires is combined and in half of individual fire plumes. This results in a strong decrease in total absorption at 405 nm and slight decrease at 660 nm with these chemical markers. These results demonstrate that changes in absorption with chemical markers of plume age are the result of decreasing OA rather than changes in the MAC of the organic material itself. While decreasing MAC or OA mass with aging could both be called bleaching, and can both correct overestimation of absorption in models, it's important to distinguish these two effects because decreasing OA mass will also decrease scattering, which will cause a significantly different net radiative effect. We also find that an average of 54% of non-BC absorption (23% total absorption) at 660 nm is from water-soluble BrC, confirming that BrC absorption is important across the visible spectrum. Quantification of significant BrC at red wavelengths and the observation of bleaching being caused by changes in OA with O:C and

37 toluene:benzene markers of plume age provide important improvements to our understanding of BrC and critical
38 constraints on aerosol absorption in regional and global climate models.

39 **1 Introduction**

40 Atmospheric aerosol impact the climate system by directly scattering and absorbing solar radiation, by
41 indirectly changing cloud properties, and through deposition that changes the surface albedo (McConnell et al., 2007;
42 Sarangi et al., 2020). Biomass burning injects a large amount of primary organic aerosol (POA), secondary organic
43 aerosol (SOA) and black carbon (BC) into the atmosphere every year. BC is somewhat poorly defined, but is generally
44 considered to be insoluble, refractory, and has an absorption exponent near one. Other materials such as elemental
45 carbon (EC), and soot (Wei et al., 2013) are often very similar to BC, but each is operationally defined by how it is
46 measured. Although it only represents a small fraction of aerosol mass, BC has a significant impact on the global
47 energy budget due to its ability to strongly absorb solar radiation at all visible wavelengths. While still important,
48 positive radiative forcing of BC is lower in IPCC AR6 (2022) than in IPCC AR5 (2013). Bond et al. (2013) estimated
49 the direct radiative forcing for BC from 1750 to 2005 at the top of the atmosphere (TOA) to be $+0.71 \text{ W m}^{-2}$, with an
50 uncertainty of 90% while the latest IPCC AR6 (2022) estimates effective radiative forcing for BC from 1750 to 2019
51 to be $+0.11$ ($-0.2 \sim +0.42$) W m^{-2} . It is important to note that AR5 reported direct radiative forcing while AR6 reports
52 effective radiative forcing. While BC is emitted from nearly all combustion processes, the largest global source of BC
53 is thought to be biomass burning (Bond et al., 2013). Organic aerosol (OA) also absorbs visible light, but its absorption
54 strongly depends on the wavelength of light (Kirchstetter and Novakov, 2004). Non-BC light absorbing organic
55 compounds are often called brown carbon (BrC) and they are usually co-emitted with BC or formed by secondary
56 chemistry in biomass burning plumes (Andreae and Gelencsér, 2006). Unlike BC, which absorbs light from the UV
57 to the IR, BrC absorption sharply increases in the UV and shorter visible portions of the spectrum and has been
58 historically considered to be almost transparent near the red wavelengths (Andreae and Gelencsér, 2006; Bahadur et
59 al., 2012; Liu et al., 2020). The global-mean TOA direct radiative forcing from BrC also shows a large uncertainty,
60 with estimates ranging from $+0.03 \text{ W m}^{-2}$ to $+0.57 \text{ W m}^{-2}$ (Saleh, 2020). Wildfires in the Western U.S. have increased
61 in recent decades (Westerling et al., 2006; Burke et al., 2021), and will continue increasing according to model
62 predictions (Yue et al., 2013; Hurteau et al., 2014; Ford et al., 2018; Neumann et al., 2021). Therefore, quantitative
63 studies of the radiative effects caused by BC and BrC emitted from wildfires are crucial for a better understanding of
64 future climate and essential to improve climate models.

65 The large uncertainty in the radiative forcing from BC is caused both by uncertainties in emissions and by
66 uncertainty in properties that affect its optics, such as size distribution, morphology, refractive index, and mixing state
67 (Bond et al., 2006; Kleinman et al., 2020; Brown et al., 2021). For wildfires, most of the aerosol mass is organic
68 (Garofalo et al., 2019). When BC is internally mixed with OA, the BC is coated by other absorbing or non-absorbing
69 materials that cause more photons to interact with the BC core, and therefore enhance the absorption of the BC core.
70 This process is often called the lensing effect even though geometric lensing is not actually happening at these sizes
71 (Fuller et al., 1999). The absorption enhancement caused by the lensing effect is defined as the ratio of the absorption
72 cross-section of a coated BC particle to that of an equivalent uncoated BC particle (Lack and Cappa, 2010). Laboratory

73 experiments have shown a strong absorption enhancement of BC by a factor of two or more (Schnaiter et al., 2003;
74 Schnaiter et al., 2005; Bond and Bergstrom, 2006; Bond et al., 2006; Peng et al., 2016). Observations of absorption
75 enhancement from ambient BC vary widely in field studies due to variations in coating thickness, coating material,
76 source type, or methodological differences, but it is often much lower than laboratory values (Liu et al., 2015, 2017;
77 Cappa et al., 2012, 2019; Healy et al., 2015; Krasowsky et al., 2016). Cappa et al. (2019) summarized absorption
78 enhancements observed at the red end of the visible spectrum from 10 studies including ambient measurements, source
79 sampling, and lab experiments. The absorption enhancement reported by those measurements ranged from 1.1 to 2.8.
80 Lack et al. (2010) found that the absorption enhancement caused by the absorbing shell would be smaller than the
81 absorption enhancement caused by the pure scattering shell. The non-spherical morphology of BC and the tendency
82 of BC to compact when coated by organics also can both enhance and decrease absorption (Romshoo et al., 2021;
83 Kelesidis et al., 2022).

84 The mass absorption cross section of BC (MAC_{BC}) is an alternative method to quantify the absorbing ability
85 of BC containing particles versus absorption enhancement. By describing the absorption per unit mass of BC, MAC_{BC}
86 can be a fundamental input in climate models to convert mass concentration into absorption coefficients (Cho et al.,
87 2019). MAC_{BC} is the particulate absorption divided by the mass of the pure BC at a certain wavelength. In this way,
88 the calculated MAC_{BC} will include absorption of the BC core along with the absorption and absorption enhancement
89 caused by the coating material. Unfortunately, the MAC of the overall BC particle, MAC_{BC} , in the ambient atmosphere
90 continues to be poorly understood due to a lack of field measurements and limitations of filter-based instruments to
91 measure this parameter. Processes that occur during atmospheric aging of BC also introduce uncertainties in its
92 absorption. Bond and Bergstrom (2006) suggested a MAC_{BC} of $7.5 \pm 1.2 \text{ m}^2 \text{ g}^{-1}$ at 550 nm for fresh BC. The following
93 campaigns demonstrate the variety of MAC_{BC} measured in the ambient during the past 15 years. Subramanian et al.
94 (2010) reported a MAC_{BC} of $10.9 \pm 2.1 \text{ m}^2 \text{ g}^{-1}$ at 660 nm and $13.1 \text{ m}^2 \text{ g}^{-1}$ at 550 nm over Mexico City when using a
95 single particle soot photometer (SP2) and the filter-based particle soot absorption photometer (PSAP) instrument
96 during airborne measurements. Krasowsky et al. (2016) reported a MAC_{BC} enhancement of 1.03 ± 0.05 due to the
97 coatings on BC. Zhang et al. (2017) found a MAC_{BC} with a mean of $10 \text{ m}^2 \text{ g}^{-1}$ and a standard deviation of $4 \text{ m}^2 \text{ g}^{-1}$ at
98 660 nm by using both SP2 and PSAP measurements. Cho et al. (2019) summarized MAC_{BC} estimated from more than
99 10 studies in East and South Asia in both ambient conditions and laboratory experiments, and the values ranged from
100 4.6 to $11.3 \text{ m}^2 \text{ g}^{-1}$.

101 The limitations of current measurement techniques bring major uncertainty into quantifying BrC absorption,
102 because BrC is usually co-emitted with BC which makes it challenging to measure BrC absorption independently.
103 BrC absorption can be directly measured through the solvent-extraction method (Peltier et al., 2007; Zeng et al., 2021;
104 Sullivan et al., 2022) or a thermodenuder (Cappa et al., 2012; Liu et al., 2015; Pokhrel et al., 2017). However, the
105 solvent-extraction method will miss BrC that's insoluble in water or organic solvents, and thermal denuders miss BrC
106 that is not volatile at the denuder temperature. BrC absorption can also be calculated from multi-wavelength total
107 absorption measurements, but this approach must assume the absorption Ångström exponent (AAE) for BC and
108 assumes that BrC does not absorb at longer wavelengths, adding significant uncertainty.

109 To improve understanding of the evolution of light-absorbing aerosol from biomass burning, smoke from 21
110 wildfires in the Western United States were measured near their sources and downwind onboard the NSF/NCAR C-
111 130 aircraft during the Western Wildfire Experiment for Cloud Chemistry, Aerosol Absorption and Nitrogen (WE-
112 CAN) campaign. This campaign represented an airborne attempt to fully characterize Western U.S. wildfires from
113 several different fuel types, locations, and fire stages (flaming vs. smoldering). This paper presents novel observations
114 about the absorbing properties of the aerosol and compares these observations to modeling studies conducted with the
115 WE-CAN data and to results from the Fire Influence on Regional to Global Environment – Air Quality (FIREX) study
116 conducted in 2019 (Zeng et al., 2021).

117 **2 Experimental Method**

118 This work relies on measurements made during the WE-CAN field campaign, which sampled smoke emitted
119 by wildfires across the Western U.S. using the NSF/NCAR C-130 research aircraft. The goal of the campaign was to
120 make detailed observations of the physical, chemical, and optical evolution of aerosol in western wildfire smoke and
121 its impact on climate, air quality, weather, and nutrient cycles. The WE-CAN field campaign consisted of 19 research
122 flights that took place from Jul. 24 – Sep. 13, 2018. Data from 13 flights where all required instrumentation was
123 available were analyzed in this study. The flight path and dominant wildfire for each of these flights are shown in Fig.
124 1. The fire locations, fuel types for each fire during WE-CAN were characterized and summarized by Lindaas et al.
125 (2021).

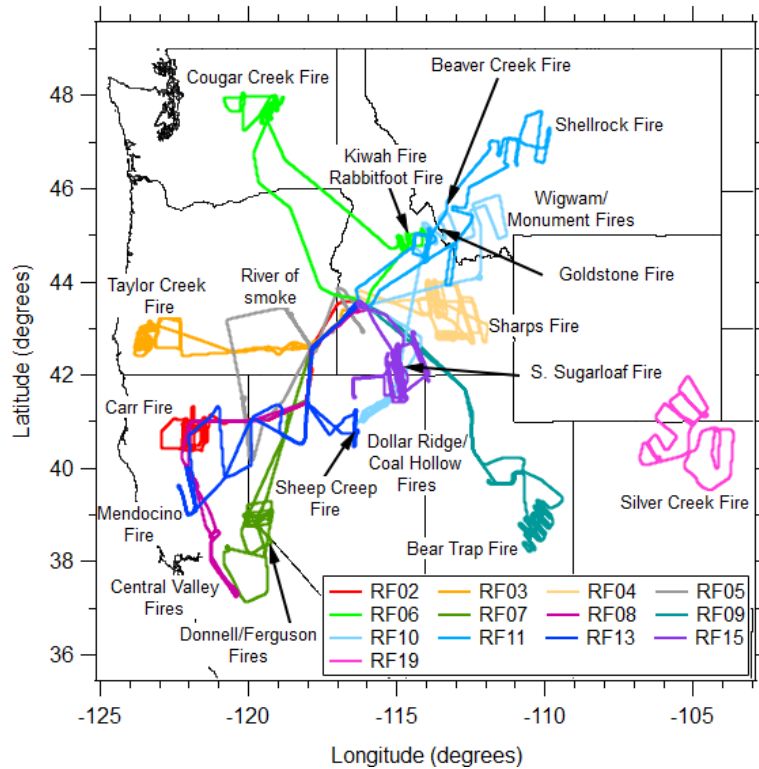


Figure 1: Flight paths and the sampled wildfires for the WE-CAN flights analyzed in this paper.

126 2.1 Instrumentation

127 The following instruments are a subset of those flown during the WE-CAN campaign and are utilized in this
 128 work. The full WE-CAN dataset is archived at https://data.eol.ucar.edu/master_lists/generated/we-can. All aerosol
 129 instruments utilized in this paper, except the PILS, pulled air from the same Solid Diffuser Inlet (SDI) inlet. The PILS
 130 sampled from a Submicron Aerosol Inlet (SMAI) (Craig et al., 2013a, 2013b, 2014; Moharreri et al., 2014). All the
 131 measurements were converted to standard temperature and pressure (STP, 1 atm, 0°C) based on the measured
 132 temperature and pressure (Eq. 1) before data were uploaded (Palm et al., 2020; Sullivan et al., 2022).

$$133 \text{ Variables}_{STP} = \text{Variables}_{measured} \cdot \frac{\text{Pressure}_{STP}}{\text{Pressure}_{measured}} \cdot \frac{\text{Temperature}_{measured}}{\text{Temperature}_{STP}} \quad (\text{Eq. 1})$$

134 2.1.1 Photoacoustic Absorption Spectrometer (PAS)

135 Aerosol absorption coefficients were measured with the multi-wavelength PAS built by the University of
 136 Wyoming (Foster et al., 2019), based on the design of Lack et al. (2012b). A PAS can directly measure the absorption
 137 coefficient of dry aerosol. The PAS represents the only way to directly measure aerosol absorption other than a
 138 photothermal interferometer (PTI, Sedlacek, 2007), which measures the change in the refractive index of the air near
 139 particles caused by heating from absorption. Briefly, when modulated laser light (at the resonant frequency of the cell)
 140 is absorbed by the aerosol it heats the surrounding air inducing pressure waves that are amplified by the cavity then
 141 detected by two microphones (Lack et al., 2006; Foster et al., 2019). The PAS used here has four cells that measure

142 the aerosol absorption coefficient from dry air at 405 nm and 660 nm and thermally denuded air at 405 nm and 660
143 nm. The denuder was set to 300°C, with the goal of evaporating volatile organic aerosol which might have a potential
144 impact on light absorption. However, absorption from the denuded channels was not used in this study, because the
145 absorption enhancement calculated using the thermodenuder approach was much smaller than the approach taking the
146 ratio of MAC_{BC} to $MAC_{BC-core}$, and we believe the discrepancy is due to the presence of significant residual organic
147 material after denuding. Two NO_x denuders coated with potassium hydroxide, guaiacol and methanol were installed
148 on the PAS in front of the inlet to remove the absorption from gas-phase NO_2 (Williams and Grosjean 1990). No
149 evidence of NO_2 absorption (which would cause baseline shifts) was observed during filter measurements that are
150 acquired every few minutes. A 3 LPM $PM_{2.5}$ cyclone (URG-2000-30ED) was used on the PAS in front of the inlet to
151 provide a $PM_{1.0}$ cut under a total flow rate of 5.7 LPM. In addition, a Nafion drier (Purma Pure PD-100T-24MPS)
152 with 100 tubes was installed on the inlet system to dry sample to a relative humidity below 30%. The particle loss (<
153 3%) in the drier was corrected during post-processing. The uncertainty in the absorption coefficient measured by the
154 PAS mainly comes from the calibration technique, in which the highly absorbing substance Regal Black and the CAPS
155 PM_{SSA} were utilized (Foster et al., 2019). The PAS was routinely calibrated (after each flight or every other day if
156 there was a flight everyday) during WE-CAN with an accuracy of +/- 10%.

157 The PAS microphone shows a pressure-dependent response to pressure. To account for this behavior, we
158 performed pressure-dependent calibration of the PAS where the instrument pressure (both PAS and CAPS PM_{SSA})
159 was dropped stepwise by ~50 torr from ambient to ~300 torr (typical minimum pressure level during WE-CAN). A
160 calibration was performed at each pressure step and the calibration constants were fitted with pressure to get a change
161 in calibration at a desired pressure. Pressure-dependent calibrations were repeated pre and post-campaign to capture
162 variability.

163 **2.1.2 Cavity-Attenuated Phase Shift Spectrometer (CAPS PM_{SSA})**

164 After pulling through the NO_x denuder, the $PM_{1.0}$ cyclone, and the Nafion drier in front of the PAS inlet, the
165 sampled air entered through the Aerodyne CAPS PM_{SSA_450} and CAPS PM_{SSA_660} to measure the aerosol scattering
166 and extinction coefficients at 450 nm and 660 nm, respectively. CAPS PM_{SSA} instruments measure extinction by
167 utilizing the cavity attenuated phase shift spectroscopy and measure scattering with an integrating sphere (Onasch et
168 al., 2015). Ammonium sulfate particles were used to calibrate the scattering channel of the CAPS PM_{SSA} during WE-
169 CAN with an accuracy of +/- 3%.

170 **2.1.3 Particle-into-Liquid Sampler (PILS) systems**

171 BrC absorption and water-soluble organic carbon (WSOC) were measured by a Particle-into-Liquid Sampler
172 (PILS) system (Sullivan et al., 2022). The PILS continuously collects ambient particles into purified water and
173 provides a liquid sample with the aerosol particles dissolved in it for analysis (Orsini et al., 2003). The size-cut for the
174 PILS was provided by a nonrotating microorifice uniform deposit impactor (MOUDI) with a 50% transmission
175 efficiency of 1 μm (aerodynamic diameter) at 1 atmosphere ambient pressure (Marple et al., 1991). The total airflow
176 for the PILS was approximately 15 LPM. Upstream of the PILS was an activated carbon parallel plate denuder

177 (Eatough et al., 1993) to remove organic gases. In addition, a valve was manually closed periodically for 10 min
178 diverting the airflow through a Teflon filter before entering the PILS allowing for background measurements. The
179 liquid sample obtained from the PILS was pushed through a 0.2 μm PTFE liquid filter by a set of syringe pumps to
180 ensure insoluble particles were removed. The flow was then directed through a liquid waveguide capillary cell (LWCC)
181 and Total Organic Carbon (TOC) Analyzer for near real-time measurement of BrC absorption and WSOC,
182 respectively. More details and a schematic illustration can be found in Zeng et al. (2021).

183 For the absorption measurement, a 2.5 m path-length LWCC (World Precision Instruments, Sarasota, FL)
184 was used. A dual deuterium and tungsten halogen light source (DH-mini, Ocean Optics, Largo, FL) and absorption
185 spectrometer (FLAME-T-UV-VIS, Ocean Optics, Largo, FL) were coupled to the LWCC via fiber optic cables.
186 Absorption spectra were recorded using the Oceanview Spectroscopy Software over a range from 200 to 800 nm. The
187 wavelength-dependent absorption was calculated following the method outlined in Hecobian et al. (2010). For this
188 study, a 16 s integrated measurement of absorption with a limit of detection (LOD) of 0.1 Mm^{-1} was obtained (Sullivan
189 et al., 2022).

190 For the WSOC measurement, a Sievers Model M9 Portable TOC Analyzer (Suez Waters Analytical
191 Instruments, Boulder, CO) was used. This analyzer works by converting the organic carbon in the liquid sample to
192 carbon dioxide through chemical oxidation involving ammonium persulfate and ultraviolet light. The carbon dioxide
193 formed was then measured by conductivity. The increase in conductivity observed was proportional to the amount of
194 organic carbon in the liquid sample. The analyzer was run in turbo mode providing a 4 s integrated measurement of
195 WSOC with a LOD of $0.1 \mu\text{g C/m}^3$ (Sullivan et al., 2022).

196 **2.1.4 Single Particle Soot Photometer (SP2)**

197 Refractory black carbon (rBC) number and mass concentrations were measured with a Single Particle Soot
198 Photometer (SP2; Droplet Measurement Technologies) which uses a continuous, 1064 nm Nd:YAG laser to heat
199 absorbing material, primarily rBC, to its vaporization temperature and measures the resulting incandescence (Schwarz
200 et al., 2006). Similar to the CAPS PM_{SSA} , the sampled air was sent through the NO_x denuder, $\text{PM}_{1.0}$ cyclone, and
201 Nafion drier in front of the PAS inlet before it went to the SP2. The SP2 was calibrated with PSL and size-selected
202 fullerene soot. On the C-130, the SP2 sample line was diluted with HEPA-filtered, pressured ambient air that was
203 passed through a mass flow controller to prevent signal saturation. During post-processing the data was corrected for
204 dilution back to ambient concentrations.

205 **2.1.5 Ultra-High Sensitivity Aerosol Spectrometer (UHSAS)**

206 Particle number concentration was measured by a rack-mounted Ultra-High Sensitivity Aerosol Spectrometer
207 (UHSAS). The flow rate of the rack-mounted UHSAS can be manually lowered by the in-flight operator when the
208 aircraft flew across smoke plumes, so that the UHSAS can stay within its optimum concentration measurement range
209 (Sullivan et al., 2022). The UHSAS was calibrated with ammonium sulfate. The particle mass concentration was
210 calculated by applying these size bins and multiplying by a particle density of 1.4 g cm^{-3} (Sullivan et al., 2022). The
211 volume mean diameter of the particles for all the detected plumes range between $0.18 \mu\text{m}$ and $0.34 \mu\text{m}$.

212 **2.1.6 Proton-Transfer-Reaction Time-of-Flight Mass Spectrometer (PTR-ToF-MS)**

213 The University of Montana proton-transfer-reaction time-of-flight mass spectrometer (PTR-ToF-MS 4000,
214 Ionicon Analytik) was utilized to report the VOC mixing ratios during WE-CAN (Permar et al., 2021). Only the
215 toluene and benzene mixing ratio derived from the PTR-ToF-MS were used in this work; their overall uncertainty is
216 < 15%. More details of the operation, calibration, and validation on the PTR-ToF-MS during WE-CAN can be found
217 in Permar et al. (2021).

218 **2.1.7 High-Resolution Aerosol Mass Spectrometry (HR-AMS)**

219 Organic aerosol (OA) was detected by the high-resolution aerosol mass spectrometry (HR-AMS; Aerodyne
220 Inc.). The description of the AMS operation during WE-CAN can be found in Garofalo et al. (2019). The atomic
221 oxygen-to-carbon ratios (O:C) and organic mass-to-organic carbon ratio (OM:OC) used in this work were determined
222 via the improved ambient elemental analysis method for the AMS (Canagaratna et al., 2015). Average (integrated)
223 elemental ratios were obtained by averaging (integrating) elemental masses of carbon, hydrogen, and oxygen and
224 recalculating elemental ratios.

225 **2.1.8 Quantum Cascade Laser (QCL) and Picarro Cavity Ring-Down spectrometer (Picarro)**

226 The carbon monoxide (CO) mixing ratio was measured by both an Aerodyne quantum cascade laser
227 instrument (CS-108 miniQCL) and a Picarro cavity ring-down spectrometer (G2401-m WS-CRD) (Garofalo et al.,
228 2019). Because the QCL has better precision than the Picarro instrument, CO measurements from the QCL were
229 preferentially used. However, CO measurements from the Picarro CO data were used for RF10 and RF13, because the
230 CO-QCL was not operated during those two flights. The carbon dioxide (CO₂) mixing ratio was also determined from
231 the Picarro.

232 **2.2 Plume Physical Age**

233 The physical age of the plume was calculated by dividing the distance the plume was sampled from the fire
234 source by the in-plume average wind speed. The average wind speed was measured on the NSF/NCAR C-130 aircraft
235 during each plume pass. The distance was estimated by using the longitude and latitude of the geometric center of the
236 plume measured on the NSF/NCAR C-130 and the fire location provided by the U.S. Forest Service. The same method
237 was used by Garofalo et al. (2019), Peng et al. (2020), Lindaas et al. (2021), Permar et al. (2021), and Sullivan et al.
238 (2022) and are also utilized here for consistency.

239 **2.3 Plume Integration Method**

240 During the WE-CAN campaign, both the SP2 and PILS had significant hysteresis compared to other
241 instruments. In the SP2 this is because the sampled air was diluted with particle-free ambient air at various ratios to
242 prevent signal saturation. In the PILS this is because of the retention effect of liquid on the wetted component or within
243 dead volumes (Zeng et al., 2021). Therefore, it was most accurate to integrate properties across airborne transects of
244 wildfire plumes to avoid the impact of instrument hysteresis and measurement noise that can dramatically impact

245 instantaneous ratios. Pseudo-Lagrangian sampling was used during the flights for the WE-CAN campaign, the C-130
 246 aircraft repeatedly crossed the smoke plume from a particular fire by traveling perpendicular to the prevailing winds,
 247 crossing the plume, turning, then crossing the plume again further downwind. In this work, we manually identified
 248 plume edges based on the inflection point when CO concentrations stopped rapidly changing as we entered and exited
 249 the smoke plume. The outside of plume measurement periods had CO mixing ratios from 100 - 300 ppbv. The lowest
 250 10% of each variable from outside plume segments were set to be the background of that variable. If the time between
 251 two consecutive outside plume segments was larger than 20 s and the highest CO mixing ratio was 100 ppbv higher
 252 than the outside plume CO criteria, this segment was chosen as a plume. The start and end point of each plume was
 253 slightly adjusted manually based on the CO mixing ratio to make sure the entire plume was covered. A different start
 254 and end point for the SP2 and PILS was adjusted manually based on the rBC mass concentrations and WSOC,
 255 respectively.

256 2.4 Absorption Enhancement and Mass Absorption Cross-section

257 Absorption enhancement (E_{abs}) is the ratio of the absorption of all particles (including BC core and coating
 258 materials) to the absorption of BC alone (Lack and Cappa, 2010). E_{abs} at 660 nm ($E_{abs,660}$) was calculated in this
 259 study by Eq. 2:

$$E_{abs,660} = \frac{Abs_{Total,660}}{M_{BC} * MAC_{BC,core,660}} \quad (Eq. 2)$$

260 where $Abs_{Total,660}$ is the total absorption coefficient at a wavelength of 660 nm measured by the PAS, M_{BC} is the
 261 mass concentration of BC measured by the SP2, and $MAC_{BC,core,660}$ is the MAC of BC alone (without any other
 262 coating material) at 660 nm, which is set to be $6.3 \text{ m}^2 \text{ g}^{-1}$ (Bond and Bergstrom, 2006; Subramanian et al., 2010).

263 MAC_{BC} at 660 nm was calculated following Eq. 3:

$$MAC_{BC,660} = \frac{Abs_{Total,660}}{M_{BC}} \quad (Eq. 3)$$

264 $MAC_{BC,660}$ is utilized more often in this study than $E_{abs,660}$ because there is not a widely accepted MAC for
 265 BC emitted from wildfire. MAC of BrC and lensing is calculated at 405 and 660 nm (Eq. 4):

$$MAC_{BrC+lensing,\lambda} = \frac{Abs_{Total,\lambda} - M_{BC} * MAC_{BC,core,\lambda}}{M_{OA}} \quad (Eq. 4)$$

266 where M_{OA} is the organic mass measured by the AMS. Again, the $MAC_{BC,core,\lambda}$ is set to be 6.3 and $10.2 \text{ m}^2 \text{ g}^{-1}$,
 267 respectively, at 660 nm and 405 nm yielding an absorption Ångström exponent (AAE, the negative slope of a
 268 logarithmic absorption coefficient against wavelength) of 0.99 for the BC core (Bond and Bergstrom, 2006;
 269 Subramanian et al., 2010; Liu, et al., 2015). It should be noted that both BrC and lensing contribute to the
 270 $MAC_{BrC+lensing,\lambda}$, and cannot be separated using this approach and $MAC_{BrC+lensing,\lambda}$ is the MAC of all organics without
 271 distinguishing absorbing and non-absorbing particles.

272 MAC of water-soluble BrC at λ nm ($MAC_{ws,BrC,\lambda}$) is calculated using Eq. 5:

$$MAC_{ws,BrC,\lambda} = \frac{Abs_{ws,BrC,\lambda}}{WSOC * (WSOM:WSOC)} \quad (Eq. 5)$$

277 where $Abs_{ws_BrC_660}$ is water-soluble light absorption and WSOC is water-soluble organic carbon mass, which are
 278 both measured by the PILS system. WSOM:WSOC ratio is set to be 1.6 (Sullivan et al., 2022). MAC_{ws_BrC} is the
 279 MAC of all water-soluble organics without distinguishing absorbing and non-absorbing particles.

280 2.5 Fractional non-BC Absorption from BrC

281 Many previous studies of BrC assume that BrC does not absorb significant amounts of light at long
 282 wavelengths (532~705 nm) (Wonaschütz et al., 2009; Lack et al., 2012a; Taylor et al., 2020; Zeng et al., 2021, Zhang
 283 et al., 2022). In this study, a PILS system was used to quantify the absorption of light for water-soluble BrC at 660
 284 nm. This absorption is not likely caused by traditional BC, which is insoluble and will be removed by the PILS
 285 impactor, the 0.2 μm filter in the PILS, and that BC over 110 nm in size will not be oxidized by the TOC analyzer
 286 (Peltier et al., 2007; Zeng et al., 2021; Sullivan et al., 2022).

287 To investigate which contributes more to absorption enhancement at 660 nm, the absorption from BrC or
 288 the lensing effect, the fractional non-BC absorption from BrC at 660 nm is calculated by Eq. 6

$$289 \text{ Fractional } Abs_{BrC} = \frac{Abs_{BrC_660}}{Abs_{Total_660} - M_{BC} * MAC_{BC_core_660}} \quad (Eq. 6)$$

290 where Abs_{Total_660} is the total absorption coefficient at 660 nm which is measured by the PAS, M_{BC} is the mass
 291 concentration of BC which is measured by the SP2, and $MAC_{BC_core_660}$ is the MAC of the BC core at 660 nm which
 292 is set to be $6.3 \text{ m}^2 \text{ g}^{-1}$ (Bond and Bergstrom, 2006; Subramanian et al., 2010). Abs_{BrC_660} is the total BrC absorption
 293 coefficient at 660 nm, which is calculated from the water-soluble light absorption provided by the PILS, where we
 294 convert absorption from water-soluble BrC to total BrC. More specifically, to convert the measured light absorption
 295 by water-soluble organics into total BrC absorption in the ambient, it had to be multiplied by two factors. The first
 296 factor converts absorption from water-soluble BrC into absorption from total BrC. This factor is obtained by taking
 297 the ratio between total particulate organic mass and water-soluble particulate organic mass (OM:WSOM). Water-
 298 soluble organic mass is calculated from the PILS WSOC data using a WSOM:WSOC (water-soluble organic mass :
 299 water-soluble organic carbon) ratio of 1.6 (Duarte et al., 2015 & 2019). Ambient organic mass is measured by the
 300 AMS or calculated from the particle size distributions measured by the UHSAS assuming the particle mass all comes
 301 from organic material with a particle density of 1.4 g cm^{-3} . Both methods are used and compared in this paper. The
 302 second factor accounts for the fact that particles absorb more light than the same substance in the bulk liquid phase.
 303 Here we use Mie theory (Bohren and Huffman, 1983) to convert absorption from BrC in aqueous solution to the
 304 absorption from BrC particles in the ambient (Liu et al., 2013; Zeng et al., 2020). The complex refractive index ($m =$
 305 $n + ik$) was put into a Mie code (implemented into Igor by Ernie R. Lewis base on Bohren and Huffman, 1983) to
 306 obtain the absorption efficiency (Q), and further used to calculate the absorption coefficient by Eq. 7 (Liu et al., 2013).
 307 The real part of the refractive index (n) is set to be 1.55, and the imaginary part is calculated by using Eq. 8 (Liu et al.,
 308 2013).

$$309 Abs(\lambda, D_p) = \frac{3}{2} \cdot \frac{Q \cdot WSOC}{D_p \cdot \rho} \quad (Eq. 7)$$

$$310 k = \frac{\rho \lambda \cdot H_2O_Abs(\lambda)}{4\pi \cdot WSOC} \quad (Eq. 8)$$

311 where λ is the wavelength, D_p is the diameter of the particle, $Abs(\lambda, D_p)$ is absorption coefficient, Q is absorption
 312 efficiency, particle density (ρ) is set to be 1.4 g cm^{-3} , $WSOC$ is the mass concentration of WSOC ($\mu\text{gC m}^{-3}$) measured
 313 by the PILS, and $H_2O_Abs(\lambda)$ is the water-soluble light absorption coefficient measured by PILS. The plume averaged
 314 particle size distribution was used in the calculation, then the absorption coefficient was calculated for each size bin
 315 of UHSAS to obtain the most accurate Mie factor for each plume.

316 The average OM:WSOM factor based on the UHSAS (UHSAS factor) for all the plumes is 2.36 with a
 317 standard deviation is 1.17. The averaged OM:WSOM based on the AMS (AMS factor) is 1.63 with a standard
 318 deviation of 0.74. The average Mie factor at 660 nm is 1.47 (standard deviation of 0.13), which is close to the factor
 319 of 1.36 found by Zeng et al. (2022) based on FIREX data. The Mie factor at 405 nm based on the WE-CAN data is
 320 also calculated, with an average of 1.83, which is similar to the factor that Zeng et al. (2022) determined at 405 nm
 321 (1.7) based on FIREX and Liu et al. (2013) determined at 450 nm (1.9) based on measurements in Atlanta.

322 Sensitivity tests were done on these factors by choosing reasonable ranges of particle density (1.1 g cm^{-3} , 1.4
 323 g cm^{-3} and 1.7 g cm^{-3}) and WSOM:WSOC ratio (1.5, 1.6 and 1.8) (Duarte et al., 2015 & 2019; Finessi, et al., 2012;
 324 Sun et al., 2011) (Table S1). Particle density only affects the Mie factor and UHSAS factor, while WSOM:WSOC
 325 ratio affects the AMS factor and UHSAS factor. As shown in Table S1, the impact of particle density on the Mie factor
 326 (both at 660 nm and 405 nm) is negligible, WSOM:WSOC is the only component that affects the AMS factor (ranging
 327 from 1.48 to 1.73), while the UHSAS factor is much more sensitive (ranging from 1.65 to 3.06) to both particle density
 328 and WSOM:WSOC. Overall, Table S1 demonstrates that none of the factors other than the UHSAS factor are sensitive
 329 to the exact parameters chosen for the calculation, giving confidence that the results presented are robust.

330 This approach assumes that water insoluble BrC has the same refractive index as water soluble BrC. This
 331 assumption would provide a lower estimation on the BrC contribution to the total absorption because Sullivan et al.
 332 (2022) found that 45% of the BrC absorption at 405 nm in WE-CAN came from water-soluble species, and Zeng et
 333 al. (2022) found that insoluble BrC absorbs more at higher wavelengths than soluble BrC, and methanol-insoluble
 334 BrC chromophores caused 87% of the light absorption at 664 nm.

335 2.6 Absorption of BrC and Water-soluble BrC

336 The bulk absorption coefficient of water-soluble BrC at a specific wavelength ($Abs_{ws_BrC\lambda}$) is measured by
 337 PILS system directly. The bulk absorption coefficient of BrC is calculated from Eq. 9:

$$338 \quad Abs_{BrC+lensing,\lambda} = Abs_{Total,\lambda} - M_{BC} * MAC_{BCcore,\lambda} \quad (Eq. 9)$$

339 where the $Abs_{Total,\lambda}$ is the total absorption coefficient measured by the PAS. MAC of the BC core is set to
 340 be 6.3 and $10.2 \text{ m}^2 \text{ g}^{-1}$, respectively, at 660 nm and 405 nm. It should be noted that both BrC and lensing contribute to
 341 the bulk absorption coefficient, and cannot be separated using this approach.

342 Then the plume integrated absorption and scattering were normalized (x/CO) by taking the ratio of
 343 background-subtracted absorption or scattering (Δx) to the background-subtracted CO mixing ratio (ΔCO) (Eq. 10),
 344 so that the changing of the normalized properties is not impacted by dilution of the plume with background air.

$$345 \quad x/CO = \frac{\Delta x}{\Delta CO} \quad (Eq. 10)$$

346 2.7 Modified Combustion Efficiency (MCE)

347 The variation of burn condition (e.g., flaming vs. smoldering) and fuel type can cause a significant difference
348 in BC emissions and changes in aerosol properties (Akagi et al., 2011; Andreae, 2019). Burn conditions can be
349 estimated with the modified combustion efficiency (MCE), defined as Eq. 11:

$$350 MCE = \frac{\Delta CO_2}{\Delta CO + \Delta CO_2} \quad (Eq. 11)$$

351 where ΔCO_2 and ΔCO are the background-subtracted CO_2 and CO mixing ratio. The background of CO_2 and CO
352 mixing ratio is obtained via the same process described in Section 2.3.

353 3 Results and Discussion

354 3.1 Comparison of WE-CAN MAC_{BrC} to Modeling Studies

355 It is challenging for climate models to simulate absorption from BrC, especially because it is highly
356 wavelength dependent and may change with chemical age (Liu et al., 2020). Recently the Saleh et al. (2014)
357 parameterization has been implemented in models in an attempt to better parameterize the imaginary part of the BrC
358 refractive index (Wang et al., 2018; Carter et al., 2021). To test how accurately the Saleh parameterization matched
359 WE-CAN data, the BC:OA ratios measured during WE-CAN were input into the Saleh parameterization, which
360 provides an imaginary part for the refractive index of BrC ($k_{BrC,\lambda}$) as a function of the BC:OA ratio. The plume
361 integrated BC:OA ratio for each plume was used in the parameterization, which gave an average k_{BrC} of 0.025, 0.013,
362 0.009, respectively, at 405 nm, 550 nm and 660nm. Mie theory (Bohren and Huffman, 1983) was then used to calculate
363 the MAC for BrC. To do the Mie calculations we assumed a real part of the refractive index of 1.7 for BrC (same as
364 Saleh et al., 2014), used volume mean diameters measured for each plume, and used an organic density of 1.4 g cm⁻³.
365 Figure 2 compares the observed $MAC_{BrC+lensing}$ (Eq. 4) and MAC_{ws_BrC} (Eq. 5) with the value calculated from the Saleh
366 parameterization with inputs from WE-CAN. In both the observations and the parameterization, the MAC_{BrC} decreases
367 as wavelength increases. However, the Saleh parameterization is always significantly larger than the observations.
368 The MAC_{BrC} from the Saleh parameterization, which does not include lensing effects, is a factor of 3.4 and 2.8 larger
369 than the observed $MAC_{BrC+lensing}$ at 405 nm and 660 nm, respectively. The range of BC:OA ratios during WE-CAN
370 (0.007~0.061) is on the very small end of the range (0.005~0.7) used in Saleh's work, and the parameterization failed
371 to capture absorbing aerosol properties for this study. The discrepancy could also be partly because the data Saleh et
372 al. used for their parameterization comes from controlled laboratory burns and not wildfires or because emissions
373 observed during WE-CAN have all undergone some near-source aging before being observed by the aircraft. It is
374 worth noting that the Saleh parameterization of MAC_{BrC} is very sensitive to organic aerosol density. If particle density
375 is increased from 1.4 g cm⁻³ to 1.7 g cm⁻³, the Saleh parameterization median MAC_{BrC} decreases to 1.6 m² g⁻¹ and 0.24
376 m² g⁻¹, respectively, at 405 nm and 660 nm (a factor of 2.8 and 2.3, respectively, compared to observed MAC_{BrC} at
377 405 nm and 660 nm). The fact that the Saleh parameterization overestimates the absorption property of biomass aerosol
378 especially for fresh emitted aerosols suggests that different parameterizations are needed for the Western U.S.. Carter
379 et al. (2021) utilized the Saleh parameterization for BrC absorption in the GEOS-Chem model and also found that the

380 Saleh model overestimated BrC absorption for WE-CAN. It was hypothesized that the overestimation was due to the
 381 lack of a bleaching process for BrC in the model and offset part of the overestimation by bringing in bleaching into
 382 the model.

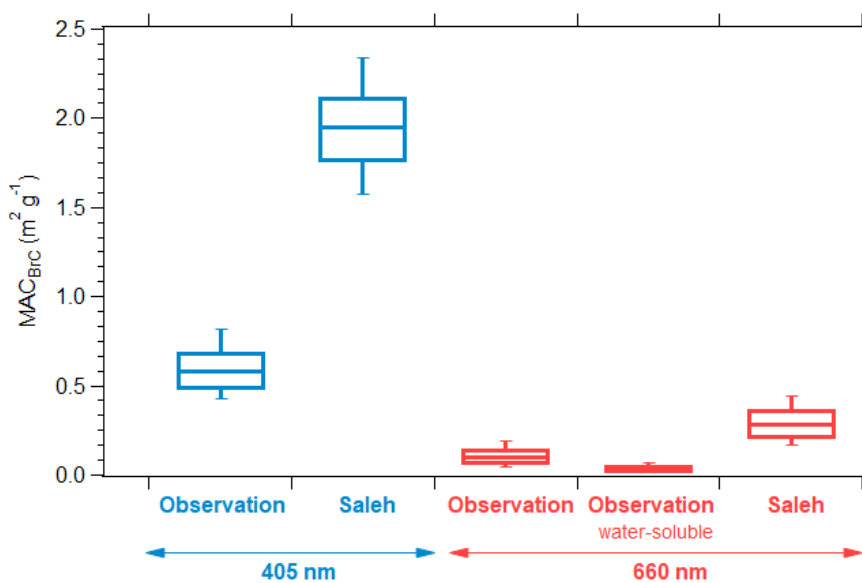


Figure 2: Boxplot summary for observed and parameterized (Saleh) MAC_{BrC} at 405 nm (blue) and 660 nm (red). For each box, the central line represents the median, the top and bottom edges represent the 75th and 25th percentile, and the top and bottom whiskers represent the 90th and 10th percentile of the data.

383 3.2 Investigation of BrC Bleaching at Visible Wavelengths

384 A limited number of field measurements have shown BrC decay with chemical age (Forrister et al., 2015;
 385 Wang et al., 2016). Despite a relatively poor understanding of the mechanism of bleaching or whitening of BrC, this
 386 process has been implemented in numerous model simulations (Brown et al., 2018; Wang et al., 2018; Carter et al.,
 387 2021). While only a fraction of organic aerosol mass absorbs light, both models and observations typically treat all
 388 organics as equally absorbing because of the inability to distinguish absorbing and non-absorbing molecules. The
 389 definition of bleaching or whitening was unclear in previous literature. Models tend to treat bleaching as the change
 390 of refractive index or decreasing of MAC (Brown et al., 2018; Wang et al., 2018; Carter et al., 2021), while
 391 observations or lab experiments mostly link bleaching to the decrease of normalized total absorption (Forrister et al.,
 392 2015; Palm et al., 2020; Zeng et al., 2022). It is important to distinguish between these two, because the decrease of
 393 absorption coefficient can also be caused by loss of absorbing organic material, which will also change the scattering
 394 coefficient and radiative forcing. Therefore, the MAC of BrC and the absorption coefficient of BrC at visible
 395 wavelengths were calculated and analyzed together with two chemical clocks (O:C and toluene:benzene ratio) and
 396 organic mass, to determine whether BrC bleached during the WE-CAN campaign, and whether the bleaching was
 397 caused by the less organic mass or the changing of refractive index. Because all large wildfire emissions are a mix of
 398 different regions that are burning slightly different fuels at different combustion efficiencies and because models treat
 399 regions, not individual fires, we identify relationships in this paper that hold true across all the flight data collected

400 during WE-CAN. These types of broad correlations are much more useful than individual case studies yielding results
401 that only hold true sometimes.

402 3.2.1 Consistency of The Mass Absorption Cross-Section of BrC at 405 nm

403 Palm et al. (2020) combined data from WE-CAN and the Monoterpene and Oxygenated aromatic Oxidation
404 at Night and under LIGHTs (MOONLIGHT) chamber experiment and found that evaporated biomass-burning POA
405 is the dominant source of biomass-burning SOA in wildfire plumes during the first a few hours after emission. They
406 also found that of the SOA formed from oxidation, phenolic compounds contribute $29 \pm 15\%$ of BrC absorption at
407 405 nm. In this section, we analyze the characteristics of BrC at 405 nm to understand the average properties of BrC
408 and to understand the balance of BrC formation versus bleaching during WE-CAN. The MAC of BrC is calculated
409 following Eq. 4 and therefore it includes a contribution from the lensing effect. The MAC of water-soluble BrC is
410 calculated following Eq. 5. Figure 3 shows the MAC of BrC at 405 nm versus the aerosol oxidation level (O:C ratio),
411 while Fig. S2 is a similar plot that uses a simple photochemical clock, the gas-phase toluene:benzene ratio. The O:C
412 ratio characterizes the oxidation state of OA and typically increases with photochemical age (Aiken et al., 2008), while
413 the toluene:benzene ratio decreases with photochemical processing time since toluene is more reactive than benzene
414 (Gouw et al., 2005). Both markers are two commonly used markers to indicate the chemical age of smoke, and they
415 correlated well with each other during WE-CAN (Fig. S1).

416 The $MAC_{BrC+lensing_405}$, varies from $0.08 \text{ m}^2 \text{ g}^{-1}$ to $1.6 \text{ m}^2 \text{ g}^{-1}$ with a mean value of $0.59 \text{ m}^2 \text{ g}^{-1}$ and a standard
417 deviation of 0.19. The largest values are from RF05, the flight through California, Oregon, and Idaho, where aged
418 smoke from different fires was mixed. The large $MAC_{BrC+lensing_405}$ occurred when the aircraft left the smoke-filled
419 boundary layer during RF05. If we exclude $MAC_{BrC+lensing_405}$ from RF05, the values range from $0.08 \text{ m}^2 \text{ g}^{-1}$ to 1.09
420 $\text{m}^2 \text{ g}^{-1}$, but still have a mean value of $0.59 \text{ m}^2 \text{ g}^{-1}$ and a standard deviation of 0.15. Again, we note that this value
421 includes the contribution of lensing. Despite this, our results lie in the same range as those measured without the
422 contribution of lensing of $0.31 \pm 0.09 \text{ m}^2 \text{ g}^{-1}$ measured in CLARIFY-2017 (Taylor, 2020), $0.13\text{-}2.0 \text{ m}^2 \text{ g}^{-1}$ measured
423 in FIREX-AQ (Zeng et al., 2022), and $0.25\text{-}1.18 \text{ m}^2 \text{ g}^{-1}$ measured in ORACLES (Zhang et al., 2022). Very weak or
424 non-trends are observed versus the chemical markers of aging (Fig. 3). If there is any trend, it is a slight increase in
425 MAC_{ws_BrC405} with O:C ratio with a poor correlation. A similar weak trend is also observed when compared
426 MAC_{ws_BrC405} and $MAC_{BrC+lensing_405}$ with the toluene:benzene ratio (Fig. S2). The flat or slightly increasing trend with
427 increasing oxidation level and decreasing toluene:benzene suggests that the refractive index of BrC is not changing in
428 a consistent way at 405 nm. It is important to remember that most of the trends observed in WE-CAN are caused by
429 emissions from different fires versus variations within a single fire, which tend to be quite small. Only 2 flights shows
430 a clear trend ($R^2 > 0.3$) for both MAC_{ws_BrC405} and $MAC_{BrC+lensing_405}$ with increasing O:C ratio at the same time, and
431 they are RF03 (R^2 of 0.85 and 0.85 with positive slope for MAC_{ws_BrC405} and $MAC_{BrC+lensing_405}$), and RF06 (R^2 of 0.8
432 and 0.49 with negative slope for MAC_{ws_BrC405} and $MAC_{BrC+lensing_405}$), where RF03 only measured a single fire (Taylor
433 Creek fire).

434

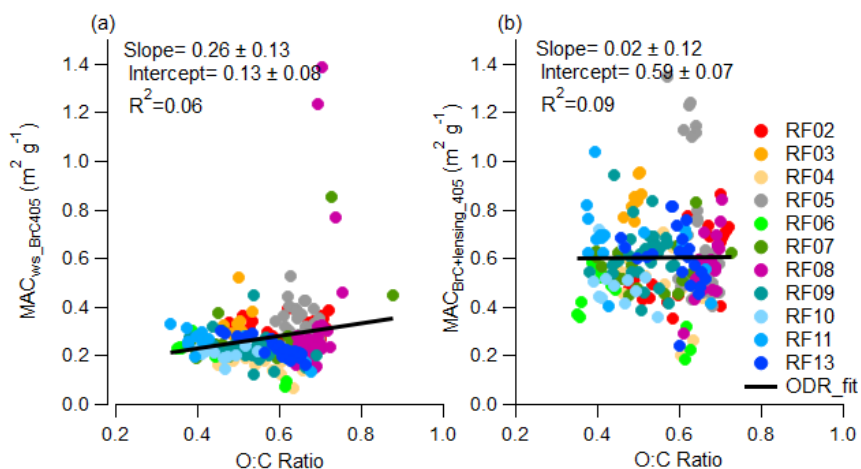


Figure 3: Plume integrated (a) MAC_{ws_BrC405} and (b) $MAC_{BrC+lensing_405}$ variations with the organic aerosol O:C ratio

435 RF05 and RF08 were chosen as case studies, to observe the optical properties of highly aged aerosol to see
 436 if the optical properties of this aerosol were similar to those observed in the near-field plume sampling of individual
 437 fires at the longest chemical or physical age observed, which was roughly 6-24 hours of physical aging. RF08 was a
 438 flight through the Central Valley of California where aged smoke from multiple fires that had settled into the valley
 439 was measured while RF05 was a flight in which smoke from several California fires was observed in California,
 440 Oregon and Idaho roughly 300~600 miles from the fires (flightpaths are shown in Fig. 1). $MAC_{BrC+lensing_405}$, CO
 441 mixing ratio, toluene:benzene ratio, and O:C ratio are displayed in Fig. 4a and 4b. The mixing ratio of CO is relatively
 442 low in these aged dilute smoke plumes vs. the plumes near the sources analyzed earlier. 1-minute averages of
 443 $MAC_{BrC+lensing_405}$ are calculated to reduce noise and 1-minute-averages for toluene:benzene ratio and O:C ratio were
 444 calculated and all the negative values were removed. As shown in Fig. 4, the smallest toluene:benzene ratio is ~0.35
 445 in RF05, and is ~0.16 in RF08, while the largest O:C ratio is ~0.7 in both RF05 and RF08, which indicates these two
 446 cases indeed captured plumes that appear chemically aged to similar extent to the other near-source flights where the
 447 smallest toluene:benzene ratio was 0.33 and the largest O:C ratio was 0.88 in near-fire measurements (Fig. 3, Fig. S2,
 448 and Fig S6a).

449 In RF05 (Fig. 4a), the weighted average O:C ratio over the entire flight was 0.64, and the toluene:benzene
 450 ratio averaged 0.45 with a standard deviation of 0.05. $MAC_{BrC+lensing_405}$ varied from $0.36 \text{ m}^2 \text{ g}^{-1}$ to $1.52 \text{ m}^2 \text{ g}^{-1}$ with an
 451 average of $0.66 \text{ m}^2 \text{ g}^{-1}$ and a standard deviation of $0.26 \text{ m}^2 \text{ g}^{-1}$. The plume that was measured in this flight was a
 452 mixture of different fire sources. Despite the much longer transit time and distance, overall these emissions, which
 453 were measured 300 to 600 miles away, have a very similar $MAC_{BrC+lensing_405}$ to that of the near-source flights where
 454 we tracked emissions from as near to the fire source as allowed by air traffic control.

455 The RF08 (Fig. 4b) results are similar to RF05, even though these emissions were smoke of mixed aged from
 456 multiple fire sources in the Central Valley of California. The weighted average O:C ratio was 0.67 over the entire
 457 measurement, and average toluene:benzene ratio was 0.41 with a standard deviation of 0.15. $MAC_{BrC+lensing_405}$
 458 averaged $0.59 \text{ m}^2 \text{ g}^{-1}$ with a standard deviation is $0.14 \text{ m}^2 \text{ g}^{-1}$. There are several extreme values that exist in the dataset,
 459 probably because of the SP2 hysteresis caused by variation in the dilution rate of the SP2 which cannot be totally

460 eliminated from the 1-minute average. In addition, the smoke from RF08 (Fig. 4b) is split into four regions based on
 461 varying observed CO mixing ratios, and integrated $MAC_{BrC+lensing_405}$ is calculated for each region (purple star marker).
 462 The regional edges are represented by blue dashed lines. Integrated $MAC_{BrC+lensing_405}$ for all of these variable CO
 463 regions is relatively stable with an average value of $0.59 \text{ m}^2 \text{ g}^{-1}$ and a standard deviation of $0.07 \text{ m}^2 \text{ g}^{-1}$.
 464

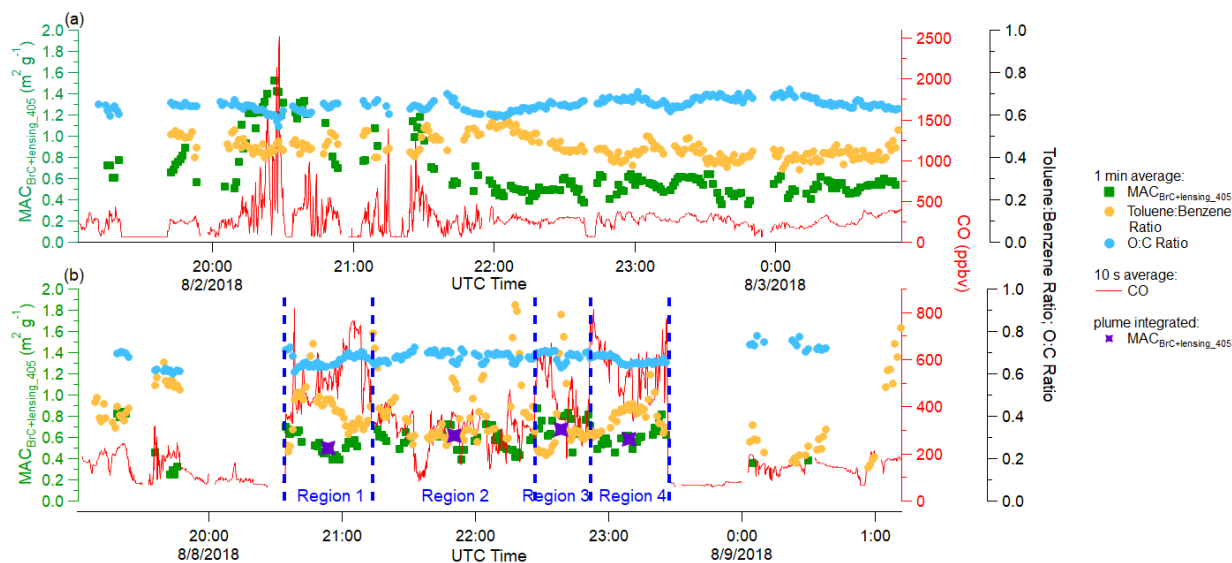


Figure 4: Time series of plume properties during (a) RF05 (measurements far from fire source), and (b) RF08 (Central Valley of California). Different square and round markers indicate 1 min averages of different variables as shown in the legend, and the red solid line represents 10 s averages of the mixing ratio of CO. Purple stars in RF08 indicate region integrated $MAC_{BrC+lensing_405}$ (individual regions are separated based on the concentration of CO, and indicated by blue dashed lines).

465 3.2.2 Decrease in Absorption at 405 nm Observed with Markers of Chemical Oxidation

466 Although neither the $MAC_{BrC+lensing_405}$ nor MAC_{ws_BrC405} decreases with O:C or Toluene:Benzenes, Fig. 5
 467 shows that BrC bleaching is observed in terms of decreased total absorption. Figure 5a and 5c show the behavior of
 468 BrC absorption at 405 nm with markers of the aerosol oxidation level (O:C) and photochemistry (toluene:benzene).
 469 The absorption coefficient of BrC shown in Fig. 5 is calculated by Eq. 9-10, which cannot separate the absorption
 470 caused by the BrC and lensing effect. To confirm that observed trends are not the result of changing lensing, the
 471 absorption coefficient of water-soluble BrC measured by the PILS, which does not include lensing effects, is also
 472 compared in Fig. 6a and 6c. The average water-soluble BrC absorption at 405 nm (Abs_{ws_BrC405} , $0.02 \text{ Mm}^{-1} \text{ ppbv}^{-1}$)
 473 which is directly measured by the PILS, is only 20% of the total absorption from BrC plus lensing ($Abs_{BrC+lensing_405}$,
 474 $0.11 \text{ Mm}^{-1} \text{ ppbv}^{-1}$), which is calculated from the PAS and SP2 (Eq.9). However, $Abs_{BrC+lensing_405}$ and Abs_{ws_BrC405}
 475 both decrease with increasing O:C ($R^2 = 0.65$ and $R^2 = 0.3$, respectively for $Abs_{BrC+lensing_405}$ and Abs_{ws_BrC405}) and
 476 decreasing toluene:benzenes ratio, which suggest a similar level of decreasing BrC absorption for all the fires observed
 477 in WE-CAN from numerous locations in the western U.S.. This relationship holds despite differences in fuel type,
 478 burn conditions, meteorology, etc. between all of these fires. The observed trends are mostly due to the decreasing of
 479 both total OA mass (Fig. 5b and 5d) and WSOC (Fig. 6b and 6d) with the increasing O:C ratio ($R^2 = 0.8$ and $R^2 = 0.4$,

480 respectively for OA and WSOC) and decreasing toluene:benzene ratio ($R^2 = 0.64$ and $R^2 = 0.44$, respectively for OA
481 and WSOC). Overall, the organic aerosol O:C ratio better predicts BrC evolution than toluene:benzene ratio, probably
482 because it is a particle-phase property rather than a gas-phase one. Again, it is important to clarify if BrC “bleaching”
483 is caused by decreasing BrC absorption coefficient or decreasing of BrC refractive index (or MAC). In this study,
484 decreasing MAC_{BrC} is not observed, rather the BrC absorption coefficient decreases significantly with the the simple
485 O:C and Toluene:Benzene chemical clocks due to loss of OA mass. Less OA mass also causes decrease in bulk
486 scattering coefficient (Fig. S3), leading to a very different net radiative effect than reducing MAC_{BrC} .

487 It is important to recall that we aimed to find general trends that hold for all fires in the western U.S., and the
488 above trend is significant when all fires are grouped together, although the trend is, in fact, not robust in each flight
489 and is rather due to variations between the fire plumes rather than variation within a single fire plume. Figure 7 shows
490 the correlation between normalized OA and chemical age for each fire source. It demonstrates that different fires show
491 different relationships and that OA does not always decrease with oxidation level/chemical aging within a single fire
492 (Kiwah fire and Rabbitfoot fire), though increasing O:C ratio does correlate well ($R^2 > 0.3$) with decreasing OA mass
493 in 7 fires (with R^2 of 0.94 for Taylor Creek fire, 0.87 for Carr fire, 0.86 for Beaver Creek fire, 0.8 for Coal Hollow
494 fire, 0.76 for Bear Trap fire, 0.35 for Sharps fire, and 0.31 for Sugarloaf fire). Toluene:benzene ratio didn’t track OA
495 as good as O:C ratio, and decreasing toluene:benzene ratio correlates well ($R^2 > 0.3$) with decreasing OA mass in 3
496 fires (with R^2 of 0.87 for Rabbitfoot fire, 0.85 for Coal Hollow fire, and 0.84 for Bear Trap fire).

497

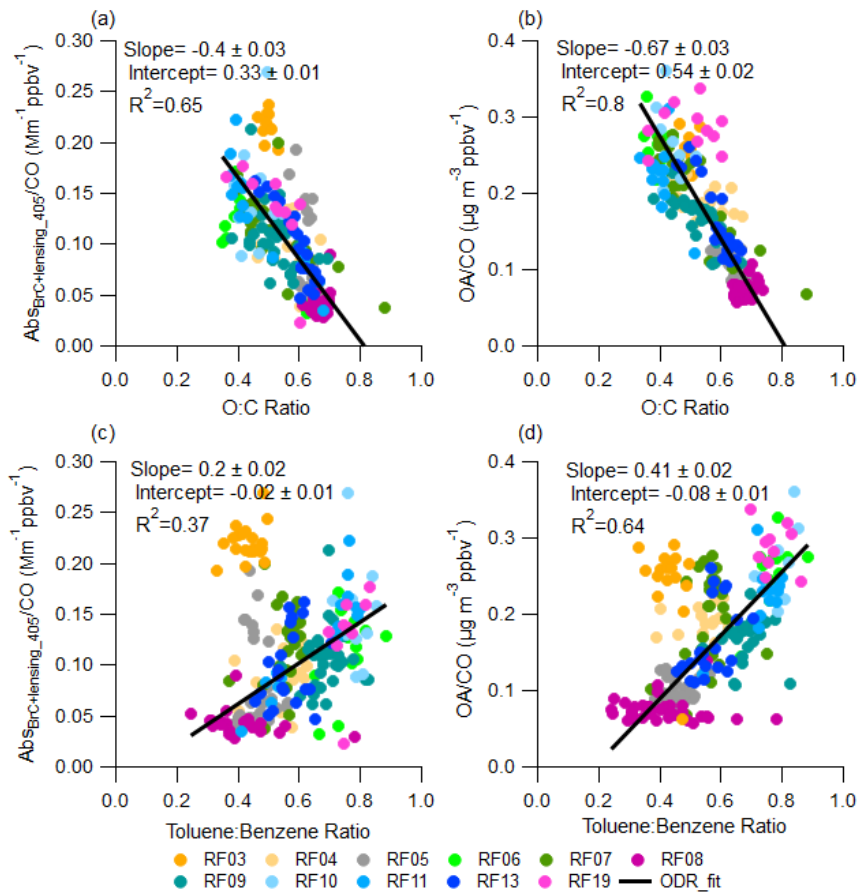


Figure 5: Plume integrated normalized $Abs_{BrC+lensing_405}$, and OA variation with chemical age. Top panels show (a) plume integrated normalized $Abs_{BrC+lensing_405}$, and (b) plume integrated normalized OA variation with O:C ratio. Bottom panels show (c) plume integrated normalized $Abs_{BrC+lensing_405}$, and (d) plume integrated normalized OA variation with toluene:benzene ratio. Data from RF03 was excluded from the ODR fit with toluene:benzene ratio, because RF03 sampled the injection of fresh smoke into the free troposphere, where gas species reacted more rapidly than particles and toluene:benzene ratio failed to keep track of aerosol evolution.

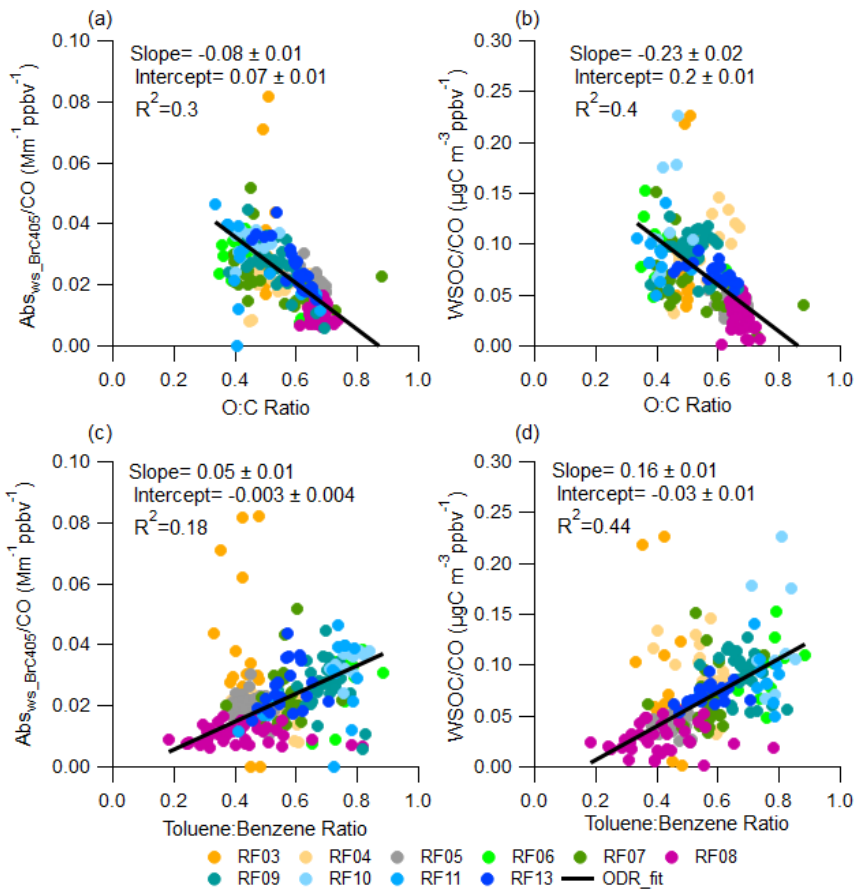


Figure 6: Similar to Fig. 5, but with plume integrated normalized Abs_{ws_BrC405} , from PILS in (a) and (c), and WSOC in (b) and (d)

499

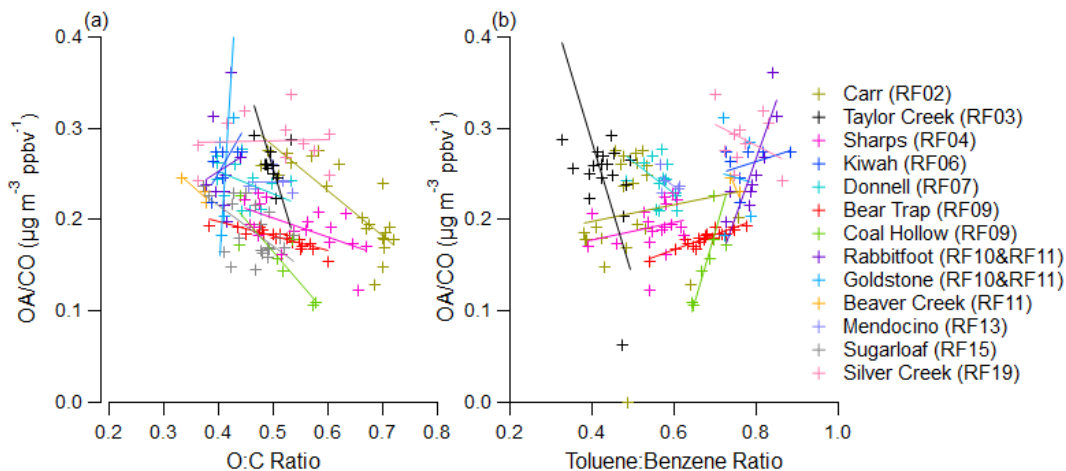


Figure 7: Plume integrated normalized OA variation with (a) O:C ratio and (b) toluene:benzene ratio. Different colors were used to distinguish plumes from different fire sources. Plumes from uncertain fire sources (especially plumes from RF05, RF08) were not included in this plot.

500

501 No trend is observed in CO normalized OA mass with plume physical age (Fig. S4), which is consistent with
502 the result from Garofalo et al. (2019) in that no net OA mass change was observed in individual plumes during WE-
503 CAN when they are characterized by physical age, although more data from additional fires were included in the
504 current work. Plume-integrated CO-normalized OA also shows weak or no trend with altitude and temperature (Fig.
505 S5). However, we note that the smallest OA:CO was captured in the plumes (RF08) that have highest temperature
506 (~305 K), and larger OA:CO tends to be observed in the colder plumes (RF19). More studies are needed to determine
507 how much OA is evaporated in high temperature plumes because the WE-CAN dataset does not capture enough
508 variation of temperature within plumes to make a robust conclusion. No clear trend was found between
509 $MAC_{BrC+lensing_405}$ and physical age or MCE (Fig. S6). Similar behavior was also observed in Western wildfires at 405
510 nm in FIREX-AQ (Zeng et al., 2022). Part of the reason is that for most fires, we only captured the first few hours (<
511 15 h), and MCE do not have a robust capability to predict biomass burning particle properties (McClure et al., 2020).
512 No trend is found between $MAC_{BrC+lensing_405}$ and altitude or temperature (Fig. S7). The trend with BC:OA ratio (Fig.
513 S8) is not as clear as in Saleh et al. (2014), most probably because the range of BC:OA ratios observed during WE-
514 CAN (0.007~0.061) is much smaller than that (0.005~0.7) observed in Saleh's work. Even in their work, the increasing
515 trend is not very clear if one only focuses on the region where the BC:OA ratio is less than 0.03. Also, the Saleh et al.
516 (2014) results were obtained from laboratory burns and not wildfires, which might also cause a discrepancy.

517 3.2.3 Mass Absorption Cross-Section and Optical Properties of BrC at 660 nm

518 BrC is defined as OA that has strong absorption at UV and shorter visible portions of the spectrum and has
519 been historically considered to be almost transparent near the red wavelengths (Andreae and Gelencsér, 2006; Bahadur
520 et al., 2012; Liu et al., 2020). However, during WE-CAN, we were able to quantify Abs_{ws_BrC660} with the PILS
521 instrument. We know that absorption observed in the PILS at 660 nm is not BC because BC is insoluble and will be
522 removed by the PILS impactor, the 0.2 μm filter in the instrument, and that BC over 110 nm in size will not be oxidized
523 by the TOC analyzer (Peltier et al., 2007; Zeng et al., 2021; Sullivan et al., 2022). Next, we investigate the behavior
524 of BrC absorption at 660 nm to see if BrC has a similar behavior at the long versus short ends of the visible spectrum.

525 Figure 8 shows the behavior of brown carbon at 660 nm vs. the O:C ratio. Similar to 405 nm, no bleaching
526 in terms of decreased MAC is observed at 660 nm. If there is any trend, it is increasing MAC_{ws_BrC660} and
527 $MAC_{BrC+lensing_660}$ with organic aerosol O:C ratio. Similar trends are observed, though with lower correlation, versus
528 the toluene:benzene ratio (Fig. S9). The mean value of $MAC_{BrC+lensing_660}$ is $0.11 \text{ m}^2 \text{ g}^{-1}$ (with a standard deviation of
529 0.06), which is much larger than the 0.03 average of MAC_{ws_BrC660} , a result we have attributed to the lensing effect,
530 but which could also partially be the result of water-insoluble BrC having a higher MAC than water-soluble BrC.

531 These results for the behavior of MAC_{BrC} at different wavelengths derived using different instruments (PAS
532 and PILS) is further evidence that MAC_{BrC} does not decrease with physical or chemical age in the WE-CAN dataset.
533 At a minimum, the plume integrated results, which represent total optical properties relevant to climate models, do
534 not capture any MAC_{BrC} decay that might be occurring at the edges of the plume.

535

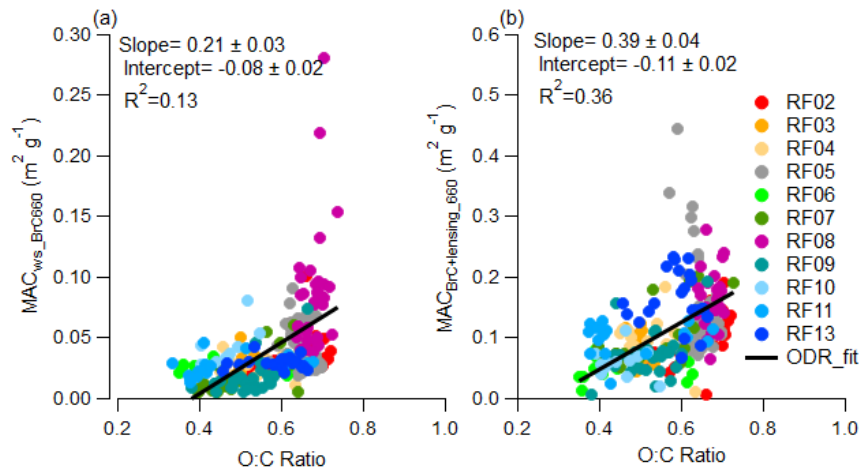


Figure 8: Plume integrated (a) MAC_{ws_BrC660} and (b) $MAC_{BrC+lensing_660}$ variations with O:C ratio

536 Similar to our analysis at 405 nm, RF05 and RF08 are presented as case studies to investigate the behavior
 537 of $MAC_{BrC+lensing_660}$ in aged plumes emitted from different fire sources. Figure 9 is similar to Fig. 4, but with
 538 $MAC_{BrC+lensing_660}$ instead of $MAC_{BrC+lensing_405}$. For the case of RF05 (Fig. 9a) $MAC_{BrC+lensing_660}$ varied from 0.04 m^2
 539 g^{-1} to $0.40 \text{ m}^2 \text{ g}^{-1}$ with an average of $0.15 \text{ m}^2 \text{ g}^{-1}$ and a standard deviation of $0.07 \text{ m}^2 \text{ g}^{-1}$. The $MAC_{BrC+lensing_660}$ tends
 540 to be larger when CO mixing ratio is higher, but does not have a significant correlation with any marker of oxidation
 541 level or photochemistry shown in Fig. 9. For the case of RF08 (Fig. 9b) $MAC_{BrC+lensing_660}$ is more stable than in RF05,
 542 and varied from $0.04 \text{ m}^2 \text{ g}^{-1}$ to $0.37 \text{ m}^2 \text{ g}^{-1}$ with an average of $0.18 \text{ m}^2 \text{ g}^{-1}$ and a standard deviation of $0.06 \text{ m}^2 \text{ g}^{-1}$. The
 543 regional integrated $MAC_{BrC+lensing_660}$ is even more stable with an average value of $0.16 \text{ m}^2 \text{ g}^{-1}$ and a standard deviation
 544 of $0.01 \text{ m}^2 \text{ g}^{-1}$. Similar to the results at 405 nm, we observe that the MAC in these very aged plumes is very similar to
 545 the average MAC observed in the near field.
 546

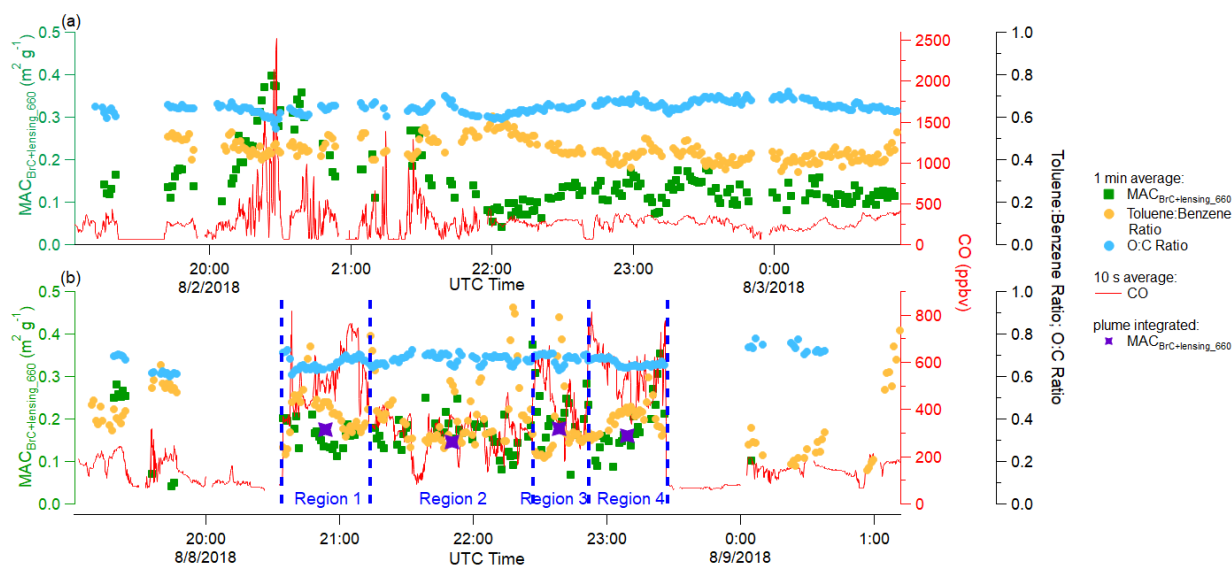


Figure 9: Time series of plume properties during (a) RF05, and (b) RF08(Central Valley of California). Different square and round markers indicate 1 min averages of different variables as shown in the legend, and the red solid line represents 10 s averages of the mixing ratio of CO. Purple stars in RF08 indicate region integrated $MAC_{BrC+lensing_660}$ (individual regions are separated based on the concentration of CO, and indicated by blue dashed lines).

547 Normalized $Abs_{BrC+lensing_660}$ and total scattering coefficient at 660 nm (Fig. S10), as well as normalized
 548 Abs_{ws_BrC660} (Fig. S11) were also investigated to see if they decreased with markers of chemical age similar to the
 549 results seen at 405 nm. However, the correlation between these BrC optical properties with O:C ratio or
 550 toluene:benzene ratio at 660 nm is much weaker and flatter than they are at 405 nm. Perhaps this is because BrC
 551 absorption is very small at 660 nm, and a large uncertainty is brought in from the assumptions required for calculation
 552 of this property and instrumental uncertainties. The average normalized $Abs_{BrC+lensing_660}$ is $0.02 \text{ Mm}^{-1} \text{ ppbv}^{-1}$, which
 553 is 5 times lower than the absorption at 405 nm; while the average normalized Abs_{ws_BrC660} is a order of magnitude
 554 lower than Abs_{ws_BrC405} . The $MAC_{BrC+lensing_660}$ (Fig. S12) shows better correlation with BC:OA ratio than
 555 $MAC_{BrC+lensing_405}$, though the increasing trend is still not as significant as Saleh et al. (2014) due to a much smaller
 556 BC:OA ratio during WE-CAN.

557 3.3 Relative Importance of BrC vs. the Lensing Effect at 660 nm

558 Plume integrated MAC_{BC} at 660 nm (MAC_{BC660}) from the 13 WE-CAN research flights with clear plume
 559 transects of biomass burning plumes are shown in Fig. 10. The MAC_{BC660} discussed in this section is calculated from
 560 Eq. 3, and has contributions from absorption from the BC core, the BrC shell, and the lensing effect. Again, even fire
 561 plumes from individually named fires are usually a mix of many different burning conditions, and it is hard to identify
 562 the exact source in most wildfire smoke measurements, especially for well mixed plumes. Therefore flight-to-flight
 563 data is analyzed because each flight covered a region, and an overall behavior of absorbing aerosol from wildfire can
 564 be provided. MAC_{BC660} varies between different flights with RF03 having the highest average MAC_{BC660} of 12.9 m^2
 565 g^{-1} , and RF10 having the lowest average MAC_{BC660} of $8.6 \text{ m}^2 \text{ g}^{-1}$. Even in highly aged plumes with emissions mixed
 566 from multiple fires (RF05 and RF08), the MAC_{BC660} is similar in magnitude and consistency with an average of 11.3

567 $\pm 1.8 \text{ m}^2 \text{ g}^{-1}$. The average of all plume-integrated $\text{MAC}_{\text{BC660}}$ is $10.9 \text{ m}^2 \text{ g}^{-1}$, with a standard deviation of $2.1 \text{ m}^2 \text{ g}^{-1}$.
 568 This result is similar to some other recent airborne measurements. Subramanian et al. (2010) reported a $\text{MAC}_{\text{BC660}}$ of
 569 $10.9 \pm 2.1 \text{ m}^2 \text{ g}^{-1}$ using a SP2 and PSAP operated during the MILAGRO campaign, which included airborne
 570 measurements of biomass burning over Mexico. Similarly, Zhang et al. (2017) estimated a $\text{MAC}_{\text{BC660}}$ of $10 \text{ m}^2 \text{ g}^{-1}$
 571 utilizing both SP2 and PSAP deployed on the NASA DC-8 research aircraft for the DC3 campaign, which measured
 572 the upper tropospheric BC over the central U.S. Taylor et al. (2020) calculated a $\text{MAC}_{\text{BC655}}$ of $12 \pm 2 \text{ m}^2 \text{ g}^{-1}$ for biomass
 573 burning emissions from Africa over the southeast Atlantic Ocean, using airborne measurements from a SP2 and PAS
 574 in the CLARIFY-2017 campaign.

575 These results are encouragingly similar given the breadth of measurement techniques (PSAP is filter-based
 576 whereas PAS is a direct measurement), geographic regions (Continental U.S. for DC3, Mexico for MILAGRO, African
 577 outflow for CLARIFY) and altitude in the atmosphere (all were airborne campaigns covering a range of altitudes). If
 578 we apply $6.3 \text{ m}^2 \text{ g}^{-1}$ as the MAC of a BC core at 660 nm (Bond and Bergstrom, 2006; Subramanian et al., 2010), then
 579 the average absorption enhancement for the entire WE-CAN campaign is 1.7. This means the absorption of coated BC
 580 is 1.7 times higher than bare BC at 660 nm, which is somewhat close to the factor of ~ 2 reported by laboratory
 581 experiments (Schnaiter et al., 2005; Peng et al., 2016), larger than some field measurements (Cappa et al., 2012&2019;
 582 Healy et al., 2015), but close to 1.85 ± 0.45 measured by Taylor et al. (2020) in African biomass burning plumes. The
 583 similarity to the Taylor et al. (2020) result suggests global similarities in the $\text{MAC}_{\text{BC660}}$ from aerosol emitted from
 584 wildfires.

585

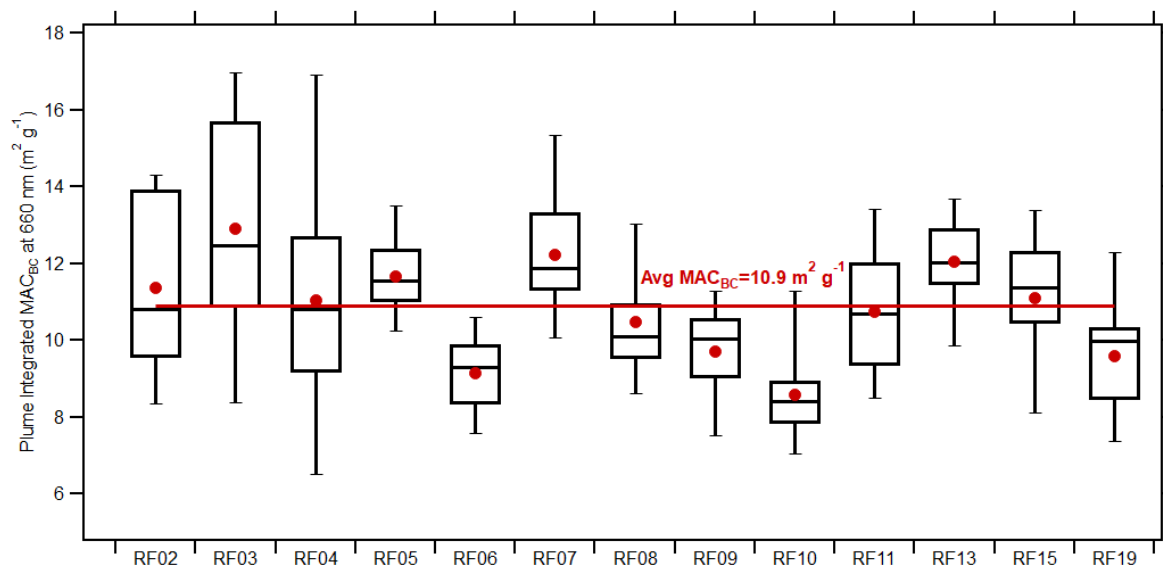


Figure 10: Box plots of plume integrated $\text{MAC}_{\text{BC660}}$ for each flight. On each box the central line represents the median, the top and bottom edges represent the 75th and 25th percentile, and the top and bottom whiskers represent the 90th and 10th percentile of the data. The red dot shows the average, and the red line indicates the average value for all plume integrated $\text{MAC}_{\text{BC660}}$.

586 MAC_{BC660} is also compared with the physical age and MCE (Fig. S13), the O:C and toluene:benzene chemical
587 clocks (Fig. S14), and the altitude, temperature and dilution (ΔCO) (Fig. S15). However, no clear trend is be found in
588 these comparisons.

589 The average absorption enhancement of 1.7 at 660 nm in this study indicates that, on average, 41% of total
590 absorption at 660 nm is caused by lensing and absorbing organics, instead of BC itself. Figure 11 shows the fraction
591 of non-BC absorption from BrC at 660 nm for the biomass burning plumes encountered during WE-CAN using Eq.
592 6-8 with OM calculated from the AMS. The figure is plotted versus plume physical age to allow visualization of the
593 variability, though there is no clear trend with physical age other than perhaps a decrease in variability with increasing
594 physical age. Figure S16 shows a similar result by using OM calculated from the UHSAS. More details on the
595 calculation and the AMS vs. UHSAS methods are explained in section 2.5. Assuming a MAC of the BC core of 6.3
596 $m^2 g^{-1}$, BrC contributes roughly the same amount of absorption at 660 nm as lensing (46% from the AMS method, 62%
597 from the UHSAS method). This means that 19% (AMS method) to 26% (UHSAS method) of the total absorption at
598 660 nm comes from BrC. When different particle density and WSOM:WSOC ratios are considered (top and bottom
599 whiskers, as well as red and blue dashed lines), the fraction of non-BC absorption is 41-49% for the AMS approach
600 (Fig. 11) and 43-80% for the UHSAS approach (Fig. S16) based on different OM:OC and density. The UHSAS
601 approach shows larger uncertainty because it's sensitive to the particle density when calculating particulate mass
602 (Table S1). While there is considerable variability between flights, a rule of thumb that roughly half of the non-BC
603 absorption at red wavelengths is from absorbing organic material seems reasonable. To the best of our knowledge, this
604 is the first observation-based attempt to differentiate between lensing and absorbing organics in the red wavelengths.
605 This approach assumes that water insoluble BrC has the same refractive index as water soluble BrC.

606

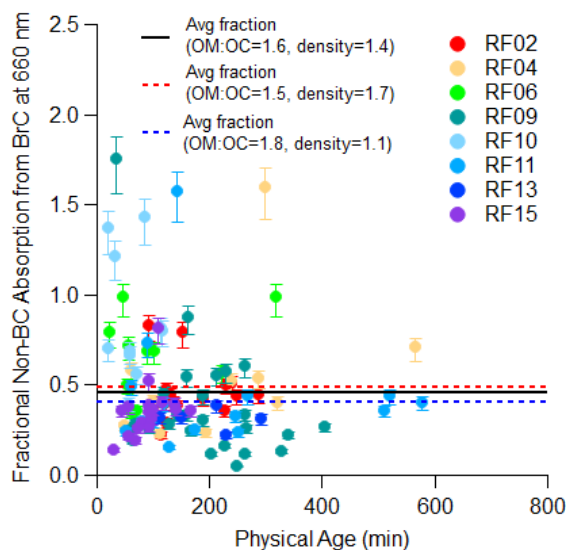


Figure 11: Time evolution of the fraction of non-BC absorption from BrC at 660 nm with AMS and Mie factor. Markers were calculated using a density of 1.4 g cm^{-3} and WSOM:WSOC ratio of 1.6. The top whiskers represent sensitive test values using a density of 1.7 g cm^{-3} and WSOM:WSOC ratio of 1.5, while the bottom whiskers represent sensitive test values using a density of 1.1 g cm^{-3} and WSOM:WSOC ratio of 1.8. The averaged fraction of non-BC absorption from BrC from all the plumes are shown in black solid lines, while the range of this result from sensitivity tests are shown in red and blue dashed lines.

607 4 Conclusion

608 In this study, we presented results that enable a better understanding of the ability of aerosol emissions from
 609 wildfires to absorb visible light and how those properties change after emission. We presented mass absorption
 610 coefficients (MAC) for BC and BrC from Western United States wildfires measured during the WE-CAN campaign
 611 at both short and long visible wavelengths ($\text{MAC}_{\text{BC}660}$, $\text{MAC}_{\text{BrC+lensing}_660}$, $\text{MAC}_{\text{ws}_\text{BrC}660}$, $\text{MAC}_{\text{BrC+lensing}_405}$). We also
 612 investigated the bulk absorption coefficient for BrC and bulk scattering coefficient for total aerosol at both short and
 613 long visible wavelengths. General trends that held for all the fire sources are derived, which should be valid throughout
 614 the western U.S. given the wide variety of emissions used to develop them.

615 By utilizing a common parameterization for BrC refractive index from Saleh et al. (2014), with measured
 616 inputs for the BC:OA ratio and particle size, we calculated the theoretical $\text{MAC}_{\text{BrC}660}$ and $\text{MAC}_{\text{BrC}405}$, and they were
 617 2.3~3.4 times larger than the measured $\text{MAC}_{\text{BrC+lensing}}$ during WE-CAN. While this discrepancy has been resolved
 618 previously by implementing bleaching into model schemes, we show that this is probably the incorrect explanation
 619 given the MAC of BrC either remains constant or slightly increases when chemical markers (O:C, toluene:benzene)
 620 suggest more oxidation has occurred. We suggest a different parameterization of the refractive index is needed to
 621 represent wildfire optical properties in the Western United States rather than using bleaching to decrease the mass
 622 absorption cross section (MAC) of the Saleh parameterization. We also note that there needs to be better terminology
 623 to distinguish between decreasing absorption caused by losses of organic aerosol mass versus decreasing absorption
 624 caused by changes in the MAC of the aerosol.

625 In the blue visible wavelengths, where BrC is more often thought about, $MAC_{BrC+lensing_405}$ is $0.59 \pm 0.19 \text{ m}^2$
626 g^{-1} and shows little variation with physical age, MCE, altitude, temperature or BC:OA ratio. There isn't any decreasing
627 trends in all the MAC_{BrC} data we obtained (MAC_{ws_BrC405} , $MAC_{BrC+lensing_405}$, MAC_{ws_BrC660} , and $MAC_{BrC+lensing_660}$)
628 with markers of chemical age (toluene:benzene, O:C), but bulk absorption of BrC does decrease with these same
629 markers. In highly aged plumes from multiple fires (RF05 and RF08), the $MAC_{BrC+lensing_405}$ has an average value of
630 $0.63 \pm 0.2 \text{ m}^2 \text{ g}^{-1}$, suggesting that brown carbon remains significantly absorbing even at relatively longer ages.

631 We find that total organic aerosol (OA) and water-soluble organic carbon (WSOC) are strongly correlated
632 with chemical markers of oxidative age. OA and WSOC (both normalized to CO) decrease with decreasing
633 toluene:benzene ratio and increasing O:C ratio. However, this phenomenon is only clearly observed when data from
634 all the observed fires is included rather than during the aging of individual fire plumes. This could mean that the fires
635 either had different emission ratios of toluene:benzene and O:C or the smoke underwent rapid secondary chemistry
636 prior to the first plume pass in WE-CAN. Regardless, the correlations are fairly robust (R^2 of 0.4 to 0.8) given the
637 many variables (MCE, fuel type, etc.) that are changing in the dataset and provide a potential link between chemical
638 markers and total organic aerosol amounts across a wide range of fires. While OA and WSOC decrease with decreasing
639 toluene:benzene or increasing O:C, MAC_{BrC} actually shows a weak increasing trend with these same markers of aging,
640 showing that while the total amount of organic aerosol is decreasing, the ability of the organic to absorb per mass is
641 staying relatively constant, or even increasing. We also found that the bulk scattering coefficient (normalized to CO)
642 decreases with decreasing toluene:benzene ratio or increasing O:C ratio due to less OA being present, which leads to
643 a very different net radiative effect than that which results from just changing the refractive index of BrC.

644 In the red visible wavelengths, where BrC is often less noticed, we observed that the MAC of BC stayed
645 relatively constant across all plumes measured and at all physical ages (ages up to 15 hours observed), with an averaged
646 MAC_{BC660} of $10.9 \pm 2.1 \text{ m}^2 \text{ g}^{-1}$ (average \pm standard deviation), which includes the contribution from both lensing effect
647 and absorbing organics. This average showed no clear trends with altitude or temperature, and we saw no evidence
648 that MAC_{BC660} is correlated to MCE. Even in highly aged plumes with emissions mixed from multiple fires (RF05
649 and RF08), the MAC_{BC660} is similar in magnitude to the near-source plumes with an average of $11.3 \pm 1.8 \text{ m}^2 \text{ g}^{-1}$. Both
650 the fact that this MAC is significantly larger than the MAC for uncoated BC (often cited to be $\sim 6.3 \text{ m}^2 \text{ g}^{-1}$) and the
651 fact that the MAC remains relatively constant across different fires and different plume ages are key insights that can
652 improve models of aerosol optical properties in wildfire emissions.

653 Through a novel use of PILS data, we find that BrC contributes 41-80% of non-BC absorption at 660 nm
654 (assuming $6.3 \text{ m}^2 \text{ g}^{-1}$ as the MAC of BC core at 660 nm). BrC contributes, on average, 26% of total absorption, but
655 the absorption cross section of water-soluble BrC is relatively small at 660 nm, with a MAC_{ws_BrC660} of $0.03 \pm 0.02 \text{ m}^2$
656 g^{-1} , which does not change with physical age, and no trend with MCE is observed. The average $MAC_{BrC+lensing_660}$
657 derived from the PAS (which includes both brown carbon absorption and lensing of black carbon) is $0.11 \pm 0.06 \text{ m}^2$
658 g^{-1} .

659 **Data Availability**

660 The WE-CAN data can be found at http://data.eol.ucar.edu/master_lists/generated/we-can/.

661 The DOI for each data set used in this work are:
662 PAS and CAPS PM_{SSA}: <https://doi.org/10.26023/K8P0-X4T3-TN06>
663 PILS1: <https://doi.org/10.26023/9H07-MD9K-430D> and <https://doi.org/10.26023/CRHY-NDT9-C30V>
664 PILS2: <https://doi.org/10.26023/7TAN-TZMD-680Y>
665 SP2: <https://doi.org/10.26023/P8R2-RAB6-N814>
666 UHSAS: <https://doi.org/10.26023/BZ4F-EAC4-290W>
667 PTR-ToF-MS: <https://doi.org/10.26023/K9F4-2CNH-EQ0W>
668 HR-AMS: <https://doi.org/10.26023/MM2Y-ZGFQ-RB0B>
669 Picarro: <https://doi.org/10.26023/NNYM-Z18J-PX0Q>
670 miniQCL: <https://doi.org/10.26023/Q888-WZRD-B70F>

671 **Author Contributions**

672 SMM designed the project. YS wrote the paper. YS, RPP, APS, EJTL, LAG, DKF, WP, LH, DWT, TC, EVF, and SMM
673 collected and analyzed data.

674 **Competing Interests**

675 The authors declare that they have no conflict of interest.

676 **Acknowledgements**

677 The 2018 WE-CAN field campaign was supported by the U.S. National Science Foundation through grants AGS-
678 1650493 (U of Wyoming), AGS-1650786 (Colorado State U), AGS-1650275 (U of Montana), AGS-1650288 (U of
679 Colorado at Boulder), and the National Oceanic and Atmospheric Administration (Award # NA17OAR4310010,
680 Colorado State U). This material is based upon study supported by the National Center for Atmospheric Research,
681 which is a major facility sponsored by the National Science Foundation under Cooperative Agreement no. 1852977.
682 The authors acknowledge support from AGS-1650493 for YS, SMM and RPP, AGS-1650786 for APS and EJTL,
683 AGS-2144896 for LH and WP, AGS-1650288 for DWT, NOAA Climate Program Office's Atmospheric Chemistry,
684 Carbon Cycle, and Climate program (Grant NA17OAR4310010) for DKF and LAG.

685

686 We sincerely thank Ernie Lewis for his work implementing Mie theory into Igor code.

687 **References**

688 Aiken, A. C., Decarlo, P. F., Kroll, J. H., Worsnop, D. R., Huffman, J. A., Docherty, K. S., Ulbrich, I. M., Mohr, C.,
689 Kimmel, J. R., Sueper, D., Sun, Y., Zhang, Q., Trimborn, A., Northway, M., Ziemann, P. J., Canagaratna, M. R.,
690 Onasch, T. B., Alfarra, M. R., Prevot, A. S. H., Dommen, J., Duplissy, J., Metzger, A., Baltensperger, U. and

691 Jimenez, J. L.: O/C and OM/OC ratios of primary, secondary, and ambient organic aerosols with high-resolution
692 time-of-flight aerosol mass spectrometry, *Environ. Sci. Technol.*, 42(12), 4478–4485, doi:10.1021/es703009q,
693 2008.

694 Akagi, S. K., Yokelson, R. J., Wiedinmyer, C., Alvarado, M. J., Reid, J. S., Karl, T., Crounse, J. D. and Wennberg, P.
695 O.: Emission factors for open and domestic biomass burning for use in atmospheric models, *Atmos. Chem. Phys.*,
696 11(9), 4039–4072, doi:10.5194/acp-11-4039-2011, 2011.

697 Andreae, M. O.: Emission of trace gases and aerosols from biomass burning – An updated assessment, *Atmos. Chem.*
698 *Phys. Discuss.*, 1–27, doi:10.5194/acp-2019-303, 2019.

699 Andreae, M. O. and Gelencsér, A.: Black carbon or brown carbon? The nature of light-absorbing carbonaceous
700 aerosols, *Atmos. Chem. Phys.*, 6, 3131–3148, doi:10.5194/acp-6-3131-2006, 2006.

701 Bahadur, R., Praveen, P. S., Xu, Y. and Ramanathan, V.: Solar absorption by elemental and brown carbon determined
702 from spectral observations, *Proc. Natl. Acad. Sci.*, 109(43), 17366–17371, doi:10.1073/pnas.1205910109, 2012.

703 Bohren, C. F. and Huffman, D. R.: *Absorption and scattering of light by small particles.*, 1983.

704 Bond, T. C. and Bergstrom, R. W.: Light absorption by carbonaceous particles: An investigative review, *Aerosol Sci.*
705 *Technol.*, 40(1), 27–67, doi:10.1080/02786820500421521, 2006.

706 Bond, T. C., Habib, G. and Bergstrom, R. W.: Limitations in the enhancement of visible light absorption due to mixing
707 state, *J. Geophys. Res. Atmos.*, 111(20), 1–13, doi:10.1029/2006JD007315, 2006.

708 Bond, T. C., Doherty, S. J., Fahey, D. W., Forster, P. M., Berntsen, T., Deangelo, B. J., Flanner, M. G., Ghan, S.,
709 Kärcher, B., Koch, D., Kinne, S., Kondo, Y., Quinn, P. K., Sarofim, M. C., Schultz, M. G., Schulz, M.,
710 Venkataraman, C., Zhang, H., Zhang, S., Bellouin, N., Guttikunda, S. K., Hopke, P. K., Jacobson, M. Z., Kaiser, J.
711 W., Klimont, Z., Lohmann, U., Schwarz, J. P., Shindell, D., Storelvmo, T., Warren, S. G. and Zender, C. S.:
712 Bounding the role of black carbon in the climate system: A scientific assessment, *J. Geophys. Res. Atmos.*, 118(11),
713 5380–5552, doi:10.1002/jgrd.50171, 2013.

714 Brown, H., Liu, X., Feng, Y., Jiang, Y., Wu, M., Lu, Z., Wu, C., Murphy, S. and Pokhrel, R.: Radiative effect and
715 climate impacts of brown carbon with the Community Atmosphere Model (CAM5), *Atmos. Chem. Phys.*, 18(24),
716 17745–17768, doi:10.5194/acp-18-17745-2018, 2018.

717 Brown, H., Liu, X., Pokhrel, R., Murphy, S., Lu, Z., Saleh, R., Mielonen, T., Kokkola, H., Bergman, T., Myhre, G.,
718 Skeie, R. B., Watson-Paris, D., Stier, P., Johnson, B., Bellouin, N., Schulz, M., Vakkari, V., Beukes, J. P., van Zyl,
719 P. G., Liu, S. and Chand, D.: Biomass burning aerosols in most climate models are too absorbing, *Nat. Commun.*,
720 12(1), 1–15, doi:10.1038/s41467-020-20482-9, 2021.

721 Burke, M., Driscoll, A., Heft-Neal, S., Xue, J., Burney, J. and Wara, M.: The changing risk and burden of wildfire in
722 the United States, *Proc. Natl. Acad. Sci. U. S. A.*, 118(2), 1–6, doi:10.1073/PNAS.2011048118, 2021.

723 Canagaratna, M. R., Jimenez, J. L., Kroll, J. H., Chen, Q., Kessler, S. H., Massoli, P., Hildebrandt Ruiz, L., Fortner,
724 E., Williams, L. R., Wilson, K. R., Surratt, J. D., Donahue, N. M., Jayne, J. T. and Worsnop, D. R.: Elemental ratio
725 measurements of organic compounds using aerosol mass spectrometry : characterization , improved calibration ,
726 and implications, *Atmos. Chem. Phys.*, 15(1), 253–272, doi:10.5194/acp-15-253-2015, 2015.

727 Cappa, C. D., Onasch, T. B., Massoli, P., Worsnop, D. R., Bates, T. S., Cross, E. S., Davidovits, P., Hakala, J., Hayden,
728 K. L., Jobson, B. T., Kolesar, K. R., Lack, D. A., Lerner, B. M., Li, S. M., Mellon, D., Nuaaman, I., Olfert, J. S.,
729 Petäjä, T., Quinn, P. K., Song, C., Subramanian, R., Williams, E. J. and Zaveri, R. A.: Radiative absorption
730 enhancements due to the mixing state of atmospheric black carbon, *Science* (80-.), 337(6098), 1078–1081,
731 doi:10.1126/science.1223447, 2012.

732 Cappa, C. D., Zhang, X., Russell, L. M., Collier, S., Lee, A. K. Y., Chen, C. L., Betha, R., Chen, S., Liu, J., Price, D.
733 J., Sanchez, K. J., McMeeking, G. R., Williams, L. R., Onasch, T. B., Worsnop, D. R., Abbatt, J. and Zhang, Q.:
734 Light Absorption by Ambient Black and Brown Carbon and its Dependence on Black Carbon Coating State for
735 Two California, USA, Cities in Winter and Summer, *J. Geophys. Res. Atmos.*, 124(3), 1550–1577,
736 doi:10.1029/2018JD029501, 2019.

737 Carter, T. S., Heald, C. L., Cappa, C. D., Kroll, J. H., Campos, T. L., Coe, H., Cotterell, M. I., Davies, N. W., Farmer,
738 D. K., Fox, C., Garofalo, L. A., Hu, L., Langridge, J. M., Levin, E. J. T., Murphy, S., Pokhrel, R., Shen, Y., Szpek,
739 K., Taylor, J. W. and Wu, H.: Investigating Carbonaceous Aerosol and its Absorption Properties from Fires in the
740 western US (WE-CAN) and southern Africa (ORACLES and CLARIFY), *J. Geophys. Res. Atmos.*, 1–28,
741 doi:10.1029/2021JD034984, 2021.

742 Chen, M., Sun, Z., Davis, J. M., Liu, Y. A., Corr, C. A. and Gao, W.: Improving the mean and uncertainty of ultraviolet
743 multi-filter rotating shadowband radiometer in situ calibration factors: Utilizing Gaussian process regression with
744 a new method to estimate dynamic input uncertainty, *Atmos. Meas. Tech.*, 12(2), 935–953, doi:10.5194/amt-12-
745 935-2019, 2019.

746 Cho, C., Kim, S. W., Lee, M., Lim, S., Fang, W., Gustafsson, Ö., Andersson, A., Park, R. J. and Sheridan, P. J.:
747 Observation-based estimates of the mass absorption cross-section of black and brown carbon and their contribution
748 to aerosol light absorption in East Asia, *Atmos. Environ.*, 212(November 2018), 65–74,
749 doi:10.1016/j.atmosenv.2019.05.024, 2019.

750 Craig, L., Moharreri, A., Schanot, A., Rogers, D. C., Dhaniyala, S., Craig, L., Anderson, B. and Dhaniyala, S.:
751 Characterizations of Cloud Droplet Shatter Artifacts in Two Airborne Aerosol Inlets, *Aerosol Sci. Technol.*, 47:6,
752 662–671, doi:10.1080/02786826.2013.780648, 2013a.

753 Craig, L., Schanot, A., Moharreri, A., Rogers, D. C. and Dhaniyala, S.: Design and Sampling Characteristics of a New
754 Airborne Aerosol Inlet for Aerosol Measurements in Clouds, *J. Atmos. Ocean. Technol.*, 30, 1123–1135,
755 doi:10.1175/JTECH-D-12-00168.1, 2013b.

756 Duarte, R. M. B. O., Freire, S. M. S. C. and Duarte, A. C.: Investigating the water-soluble organic functionality of
757 urban aerosols using two-dimensional correlation of solid-state ¹³C NMR and FTIR spectral data, *Atmos. Environ.*,
758 116, 245–252, doi:10.1016/j.atmosenv.2015.06.043, 2015.

759 Duarte, R. M. B. O., Piñeiro-Iglesias, M., López-Mahía, P., Muniategui-Lorenzo, S., Moreda-Piñeiro, J., Silva, A. M.
760 S. and Duarte, A. C.: Comparative study of atmospheric water-soluble organic aerosols composition in contrasting
761 suburban environments in the Iberian Peninsula Coast, *Sci. Total Environ.*, 648, 430–441,
762 doi:10.1016/j.scitotenv.2018.08.171, 2019.

763 Eatough, D. J., Wadsworth, A., Eatough, D. A., Crawford, J. W., Hansen, L. D. and Lewis, E. A.: A multiple-system,
764 multi-channel diffusion denuder sampler for the determination of fine-particulate organic material in the
765 atmosphere, *Atmos. Environ. Part A, Gen. Top.*, 27(8), 1213–1219, doi:10.1016/0960-1686(93)90247-V, 1993.

766 Finessi, E., Decesari, S., Paglione, M., Giulianelli, L., Carbone, C., Gilardoni, S., Fuzzi, S., Saarikoski, S., Raatikainen,
767 T., Hillamo, R., Allan, J., Mentel, T. F., Tiitta, P., Laaksonen, A., Petäjä, T., Kulmala, M., Worsnop, D. R. and
768 Facchini, M. C.: Determination of the biogenic secondary organic aerosol fraction in the boreal forest by NMR
769 spectroscopy, *Atmos. Chem. Phys.*, 12(2), 941–959, doi:10.5194/acp-12-941-2012, 2012.

770 Ford, B., Val Martin, M., Zelasky, S. E., Fischer, E. V., Anenberg, S. C., Heald, C. L. and Pierce, J. R.: Future Fire
771 Impacts on Smoke Concentrations, Visibility, and Health in the Contiguous United States, *GeoHealth*, 2(8), 229–
772 247, doi:10.1029/2018gh000144, 2018.

773 Forrister, Haviland; Liu, Jiumeng; Scheuer, Eric; Dibb, Jack; Ziemba, Luke; Thornhill, L. Kenneth; Anderson, Bruce;
774 Diskin, Glenn; Perring, E. Anne; P. Schwarz, Joshua; Campuzano-Jost, Pedro; A. Day, Douglas; B. Palm, Brett;
775 Jimenez, L. Jose; Nenes, Athan, R. J.: Evolution of brown carbon in wildfire plumes, *Geophys. Res. Lett.*, 42,
776 4623–4630, doi:10.1002/2015GL063897, 2015.

777 Foster, K., Pokhrel, R., Burkhart, M. and Murphy, S.: A novel approach to calibrating a photoacoustic absorption
778 spectrometer using polydisperse absorbing aerosol, *Atmos. Meas. Tech.*, 12(6), 3351–3363, doi:10.5194/amt-12-
779 3351-2019, 2019.

780 Fuller, K. A. and Kreidenweis, S. M.: Effects of mixing on extinction by carbonaceous particles, *J. Geophys. Res.*,
781 104(D13), 15941–15954, doi:10.1029/1998JD100069, 1999.

782 Garofalo, L. A., Pothier, M. A., Levin, E. J. T., Campos, T., Kreidenweis, S. M. and Farmer, D. K.: Emission and
783 Evolution of Submicron Organic Aerosol in Smoke from Wildfires in the Western United States, *ACS Earth Sp.*
784 *Chem.*, 3(7), 1237–1247, doi:10.1021/acsearthspacechem.9b00125, 2019.

785 Gouw, J. A. De, Middlebrook, A. M., Warneke, C., Goldan, P. D., Kuster, W. C., Roberts, J. M., Fehsenfeld, F. C.,
786 Worsnop, D. R., Canagaratna, M. R., Pszenny, A. A. P., Keene, W. C., Marchewka, M., Bertman, S. B. and Bates,
787 T. S.: Budget of organic carbon in a polluted atmosphere : Results from the New England Air Quality Study in
788 2002, *J. Geophys. Res.*, 110, 1–22, doi:10.1029/2004JD005623, 2005.

789 Grieshop, A. P., Logue, J. M., Donahue, N. M. and Robinson, A. L.: Laboratory investigation of photochemical
790 oxidation of organic aerosol from wood fires 1: Measurement and simulation of organic aerosol evolution, *Atmos.*
791 *Chem. Phys.*, 9(4), 1263–1277, doi:10.5194/acp-9-1263-2009, 2009.

792 Healy, R. M., Wang, J. M., Jeong, C. H., Lee, A. K. Y., Willis, M. D., Jaroudi, E., Zimmerman, N., Hilker, N., Murphy,
793 M., Eckhardt, S., Stohl, A., Abbatt, J. P. D., Wenger, J. C. and Evans, G. J.: Light-absorbing properties of ambient
794 black carbon and brown carbon from fossil fuel and biomass burning sources, *J. Geophys. Res. Atmos.*, 120(13),
795 6619–6633, doi:10.1002/2015JD023382, 2015.

796 Hecobian, A., Zhang, X., Zheng, M., Frank, N., Edgerton, E. S. and Weber, R. J.: Water-soluble organic aerosol
797 material and the light-absorption characteristics of aqueous extracts measured over the Southeastern United States,
798 *Atmos. Chem. Phys.*, 10(13), 5965–5977, doi:10.5194/acp-10-5965-2010, 2010.

799 Hurteau, M. D., Westerling, A. L., Wiedinmyer, C. and Bryant, B. P.: Projected effects of climate and development on
800 California wildfire emissions through 2100, *Environ. Sci. Technol.*, 48(4), 2298–2304, doi:10.1021/es4050133,
801 2014.

802 Kelesidis, G. A., Neubauer, D., Fan, L. S., Lohmann, U. and Pratsinis, S. E.: Enhanced Light Absorption and Radiative
803 Forcing by Black Carbon Agglomerates, *Environ. Sci. Technol.*, 56(12), 8610–8618, doi:10.1021/acs.est.2c00428,
804 2022.

805 Kirchstetter, T. W., Novakov, T. and Hobbs, P. V.: Evidence that the spectral dependence of light absorption by aerosols
806 is affected by organic carbon, *J. Geophys. Res. D Atmos.*, 109(21), 1–12, doi:10.1029/2004JD004999, 2004.

807 Krasowsky, T. S., McMeeking, G. R., Wang, D., Sioutas, C. and Ban-Weiss, G. A.: Measurements of the impact of
808 atmospheric aging on physical and optical properties of ambient black carbon particles in Los Angeles, *Atmos.*
809 *Environ.*, 142, 496–504, doi:10.1016/j.atmosenv.2016.08.010, 2016.

810 Lack, D. A., Lovejoy, E. R., Baynard, T., Pettersson, A. and Ravishankara, A. R.: Aerosol Absorption Measurement
811 using Photoacoustic Spectroscopy: Sensitivity, Calibration, and Uncertainty Developments, *Aerosol Sci. Technol.*,
812 40(9), 697–708, doi:10.1080/02786820600803917, 2006.

813 Lack, D. A. and Cappa, C. D.: Impact of brown and clear carbon on light absorption enhancement, single scatter
814 albedo and absorption wavelength dependence of black carbon, *Atmos. Chem. Phys.*, 10(9), 4207–4220,
815 doi:10.5194/acp-10-4207-2010, 2010.

816 Lack, D. A., Langridge, J. M., Bahreini, R., Cappa, C. D., Middlebrook, A. M. and Schwarz, J. P.: Brown carbon and
817 internal mixing in biomass burning particles, *Proc. Natl. Acad. Sci. U. S. A.*, 109(37), 14802–14807,
818 doi:10.1073/pnas.1206575109, 2012a.

819 Lack, D. A., Richardson, M. S., Law, D., Langridge, J. M., Cappa, C. D., McLaughlin, R. J. and Murphy, D. M.:
820 Aircraft Instrument for Comprehensive Characterization of Aerosol Optical Properties, Part 2: Black and Brown
821 Carbon Absorption and Absorption Enhancement Measured with Photo Acoustic Spectroscopy, *Aerosol Sci.*
822 *Technol.*, 46(5), 555–568, doi:10.1080/02786826.2011.645955, 2012b.

823 Lindaas, J., Pollack, I. B., Garofalo, L. A., Pothier, M. A., Farmer, D. K., Kreidenweis, S. M., Campos, T. L., Flocke,
824 F., Weinheimer, A. J., Montzka, D. D., Tyndall, G. S., Palm, B. B., Peng, Q., Thornton, J. A., Permar, W., Wielgasz,
825 C., Hu, L., Ottmar, R. D., Restaino, J. C., Hudak, A. T., Ku, I. T., Zhou, Y., Sive, B. C., Sullivan, A., Collett, J. L.
826 and Fischer, E. V.: Emissions of Reactive Nitrogen From Western U.S. Wildfires During Summer 2018, *J. Geophys.*
827 *Res. Atmos.*, 126(2), 1–21, doi:10.1029/2020JD032657, 2021.

828 Liu, D., Whitehead, J., Alfara, M. R., Reyes-villegas, E., Spracklen, D. V., Reddington, C. L., Kong, S., Williams, P.
829 I., Ting, Y., Haslett, S., Taylor, J. W., Flynn, M. J., Morgan, W. T., Mcfiggans, G., Coe, H. and Allan, J. D.: Black-
830 carbon absorption enhancement in the atmosphere determined by particle mixing state, *Nat. Geosci.*, 10(3), 184–
831 188, doi:10.1038/NGEO2901, 2017.

832 Liu, D., He, C., Schwarz, J. P. and Wang, X.: Lifecycle of light-absorbing carbonaceous aerosols in the atmosphere,
833 *npj Clim. Atmos. Sci.*, 3(40), doi:10.1038/s41612-020-00145-8, 2020.

834 Liu, J., Bergin, M., Guo, H., King, L., Kotra, N., Edgerton, E. and Weber, R. J.: Size-resolved measurements of brown
835 carbon in water and methanol extracts and estimates of their contribution to ambient fine-particle light absorption,
836 *Atmos. Chem. Phys.*, 13(24), 12389–12404, doi:10.5194/acp-13-12389-2013, 2013.

837 Liu, S., Aiken, A. C., Gorkowski, K., Dubey, M. K., Cappa, C. D., Williams, L. R., Herndon, S. C., Massoli, P., Fortner,
838 E. C., Chhabra, P. S., Brooks, W. A., Onasch, T. B., Jayne, J. T., Worsnop, D. R., China, S., Sharma, N., Mazzoleni,
839 C., Xu, L., Ng, N. L., Liu, D., Allan, J. D., Lee, J. D., Fleming, Z. L., Mohr, C., Zotter, P., Szidat, S. and Prévôt,
840 A. S. H.: Enhanced light absorption by mixed source black and brown carbon particles in UK winter, *Nat.*
841 *Commun.*, 6, 8435, doi:10.1038/ncomms9435, 2015.

842 Marple, V. A., Rubow, K. L. and Behm, S. M.: A microorifice uniform deposit impactor (moudi): Description,
843 calibration, and use, *Aerosol Sci. Technol.*, 14(4), 434–436, doi:10.1080/02786829108959504, 1991.

844 McClure, C. D., Lim, C. Y., Hagan, D. H., Kroll, J. H. and Cappa, C. D.: Biomass-burning-derived particles from a
845 wide variety of fuels - Part 1: Properties of primary particles, *Atmos. Chem. Phys.*, 20(3), 1531–1547,
846 doi:10.5194/acp-20-1531-2020, 2020.

847 McConnell, J. R., Edwards, R., Kok, L. G., Flanner, M. G., Zender, C. S., Saltzman, E. S., Banta, J. R., Pasteris, D.
848 R., Carter, M. M. and Kahl, J. D. W.: 20th-Century Industrial Black Carbon Emissions Altered Arctic Climate
849 Forcing, *Science* (80-.), 317(5843), 1381–1384, doi:10.1126/science.1144856, 2007.

850 Moharreri, A., Craig, L., Dubey, P., Rogers, D. C. and Dhaniyala, S.: Aircraft testing of the new Blunt-body Aerosol
851 Sampler (BASE), *Atmos. Meas. Tech.*, 7(9), 3085–3093, doi:10.5194/amt-7-3085-2014, 2014.

852 Neumann, J. E., Amend, M., Anenberg, S., Kinney, P. L., Sarofim, M., Martinich, J., Lukens, J., Xu, J. W. and Roman,
853 H.: Estimating PM_{2.5}-related premature mortality and morbidity associated with future wildfire emissions in the
854 western US, *Environ. Res. Lett.*, 16(3), doi:10.1088/1748-9326/abe82b, 2021.

855 Onasch, T. B., Massoli, P., Keabian, P. L., Hills, F. B., Bacon, F. W. and Freedman, A.: Single scattering albedo
856 monitor for airborne particulates, *Aerosol Sci. Technol.*, 49(4), 267–279, doi:10.1080/02786826.2015.1022248,
857 2015.

858 Orsini, D. A., Ma, Y., Sullivan, A., Sierau, B., Baumann, K. and Weber, R. J.: Refinements to the particle-into-liquid
859 sampler (PILS) for ground and airborne measurements of water soluble aerosol composition, *Atmos. Environ.*,
860 37(9–10), 1243–1259, doi:10.1016/S1352-2310(02)01015-4, 2003.

861 Palm, B. B., Peng, Q., Fredrickson, C. D., Lee, B. H., Garofalo, L. A., Pothier, M. A., Kreidenweis, S. M., Farmer, D.
862 K., Pokhrel, R. P., Shen, Y., Murphy, S. M., Permar, W., Hu, L., Campos, T. L., Hall, S. R., Ullmann, K., Zhang,
863 X., Flocke, F., Fischer, E. V. and Thornton, J. A.: Quantification of organic aerosol and brown carbon evolution in
864 fresh wildfire plumes, *Proc. Natl. Acad. Sci. U. S. A.*, 117(47), 29469–29477, doi:10.1073/pnas.2012218117, 2020.

865 Peltier, R. E., Weber, R. J. and Sullivan, A. P.: Investigating a liquid-based method for online organic carbon detection
866 in atmospheric particles, *Aerosol Sci. Technol.*, 41(12), 1117–1127, doi:10.1080/02786820701777465, 2007.

867 Peng, J., Hu, M., Guo, S., Du, Z., Zheng, J., Shang, D., Zamora, M. L., Zeng, L., Shao, M., Wu, Y. S., Zheng, J., Wang,
868 Y., Glen, C. R., Collins, D. R., Molina, M. J. and Zhang, R.: Markedly enhanced absorption and direct radiative
869 forcing of black carbon under polluted urban environments, *Proc. Natl. Acad. Sci. U. S. A.*, 113(16), 4266–4271,
870 doi:10.1073/pnas.1602310113, 2016.

871 Permar, W., Wang, Q., Selimovic, V., Wielgasz, C., Yokelson, R. J., Hornbrook, R. S., Hills, A. J., Apel, E. C., Ku, I.
872 T., Zhou, Y., Sive, B. C., Sullivan, A. P., Collett, J. L., Campos, T. L., Palm, B. B., Peng, Q., Thornton, J. A.,
873 Garofalo, L. A., Farmer, D. K., Kreidenweis, S. M., Levin, E. J. T., DeMott, P. J., Flocke, F., Fischer, E. V. and Hu,
874 L.: Emissions of Trace Organic Gases From Western U.S. Wildfires Based on WE-CAN Aircraft Measurements,
875 *J. Geophys. Res. Atmos.*, 126(11), doi:10.1029/2020JD033838, 2021.

876 Pokhrel, R. P., Wagner, N. L., Langridge, J. M., Lack, D. A., Jayarathne, T., Stone, E. A., Stockwell, C. E., Yokelson,
877 R. J. and Murphy, S. M.: Parameterization of single-scattering albedo (SSA) and absorption Ångström exponent
878 (AAE) with EC/OC for aerosol emissions from biomass burning, *Atmos. Chem. Phys.*, 16(15), 9549–9561,
879 doi:10.5194/acp-16-9549-2016, 2016.

880 Pokhrel, R. P., Beamesderfer, E. R., Wagner, N. L., Langridge, J. M., Lack, D. A., Jayarathne, T., Stone, E. A.,
881 Stockwell, C. E., Yokelson, R. J. and Murphy, S. M.: Relative importance of black carbon, brown carbon, and
882 absorption enhancement from clear coatings in biomass burning emissions, *Atmos. Chem. Phys.*, 17(8), 5063–
883 5078, doi:10.5194/acp-17-5063-2017, 2017.

884 Romshoo, B., Müller, T., Pfeifer, S., Saturno, J., Nowak, A., Ciupek, K., Quincey, P. and Wiedensohler, A.: Optical
885 properties of coated black carbon aggregates: Numerical simulations, radiative forcing estimates, and size-resolved
886 parameterization scheme, *Atmos. Chem. Phys.*, 21(17), 12989–13010, doi:10.5194/acp-21-12989-2021, 2021.

887 Rosencwaig, A.: Photoacoustic spectroscopy., *Annu. Rev. Biophys. Bioeng.*, 9, 31–54,
888 doi:10.1146/annurev.bb.09.060180.000335, 1980.

889 Saleh, R., Robinson, E. S., Tkacik, D. S., Ahern, A. T., Liu, S., Aiken, A. C., Sullivan, R. C., Presto, A. A., Dubey, M.
890 K., Yokelson, R. J., Donahue, N. M. and Robinson, A. L.: Brownness of organics in aerosols from biomass burning
891 linked to their black carbon content, *Nat. Geosci.*, 7(9), 647–650, doi:10.1038/ngeo2220, 2014.

892 Saleh, R.: From Measurements to Models: Toward Accurate Representation of Brown Carbon in Climate Calculations,
893 *Curr. Pollut. Reports*, 6(2), 90–104, doi:10.1007/s40726-020-00139-3, 2020.

894 Sarangi, C., Qian, Y., Rittger, K., Leung, R. L., Chand, D., Bormann, K. J. and Painter, T. H.: Dust dominates high-
895 altitude snow darkening and melt over high-mountain Asia, *Nat. Clim. Chang.*, (October), 1–7,
896 doi:10.1038/s41558-020-00909-3, 2020.

897 Schnaiter, M., Horvath, H., Möhler, O., Naumann, K. H., Saathoff, H. and Schöck, O. W.: UV-VIS-NIR spectral optical
898 properties of soot and soot-containing aerosols, *J. Aerosol Sci.*, 34(10), 1421–1444, doi:10.1016/S0021-
899 8502(03)00361-6, 2003.

900 Schnaiter, M., Linke, C., Möhler, O., Naumann, K. H., Saathoff, H., Wagner, R., Schurath, U. and Wehner, B.:
901 Absorption amplification of black carbon internally mixed with secondary organic aerosol, *J. Geophys. Res. D*
902 *Atmos.*, 110(19), 1–11, doi:10.1029/2005JD006046, 2005.

903 Schwarz, J. P., Gao, R. S., Fahey, D. W., Thomson, D. S., Watts, L. A., Wilson, J. C., Reeves, J. M., Darbeheshti, M.,
904 Baumgardner, D. G., Kok, G. L., Chung, S. H., Schulz, M., Hendricks, J., Lauer, A., Ka, B., Slowik, J. G., Rosenlof,
905 K. H., Thompson, T. L., Langford, A. O., Loewenstein, M. and Aikin, K. C.: Single-particle measurements of
906 midlatitude black carbon and light-scattering aerosols from the boundary layer to the lower stratosphere, *J.*
907 *Geophys. Res.*, 111, D16207, doi:10.1029/2006JD007076, 2006.

908 Subramanian, R., Kok, G. L., Baumgardner, D., Clarke, A., Shinozuka, Y., Campos, T. L., Heizer, C. G., Stephens, B.
909 B., De Foy, B., Voss, P. B. and Zaveri, R. A.: Black carbon over Mexico: The effect of atmospheric transport on
910 mixing state, mass absorption cross-section, and BC/CO ratios, *Atmos. Chem. Phys.*, 10(1), 219–237,
911 doi:10.5194/acp-10-219-2010, 2010.

912 Sullivan, A. P., Pokhrel, R. P., Shen, Y., Murphy, S. M., Toohey, D. W., Campos, T., Lindaas, J., Fischer, E. V. and
913 Collett, J. L.: Examination of Brown Carbon Absorption from Wildfires in the Western U.S. During the WE-CAN
914 Study, *Atmos. Chem. Phys. Discuss.*, (July), 1–29, doi:10.5194/acp-2022-459, 2022.

915 Sun, Y., Zhang, Q., Zheng, M., Ding, X., Edgerton, E. S. and Wang, X.: Characterization and source apportionment
916 of water-soluble organic matter in atmospheric fine particles (PM_{2.5}) with high-resolution aerosol mass
917 spectrometry and GC-MS, *Environ. Sci. Technol.*, 45(11), 4854–4861, doi:10.1021/es200162h, 2011.

918 Szopa, S., V. Naik, B. Adhikary, P. Artaxo, T. Berntsen, W.D. Collins, S. Fuzzi, L. Gallardo, A. Kiendler-Scharr, Z.
919 Klimont, H. Liao, N. Unger, and P. Zanis: Short-Lived Climate Forcers. In *Climate Change 2021: The Physical
920 Science Basis. Contribution of Working Group I to the Sixth Assessment Report of the Intergovernmental Panel
921 on Climate Change*. Cambridge University Press, Cambridge, United Kingdom and New York, NY, USA, pp. 817–
922 922, doi:10.1017/9781009157896.008, 2021.

923 Tasoglou, A., Louvaris, E., Florou, K., Liangou, A., Karnezi, E., Kaltsonoudis, C., Wang, N. and Pandis, S. N.: Aerosol
924 light absorption and the role of extremely low volatility organic compounds, *Atmos. Chem. Phys.*, 20(19), 11625–
925 11637, doi:10.5194/acp-20-11625-2020, 2020.

926 Taylor, J. W., Wu, H., Szpek, K., Bower, K., Crawford, I., Flynn, M. J., Williams, P. I., Dorsey, J., Langridge, J. M.,
927 Cotterell, M. I., Fox, C., Davies, N. W., Haywood, J. M. and Coe, H.: Absorption closure in highly aged biomass
928 burning smoke, *Atmos. Chem. Phys.*, 20(19), 11201–11221, doi:10.5194/acp-20-11201-2020, 2020.

929 Wang, X., Sedlacek, A. J., DeSá, S. S., Martin, S. T., Alexander, M. L., Alexander, M. L., Watson, T. B., Aiken, A. C.,
930 Springston, S. R. and Artaxo, P.: Deriving brown carbon from multiwavelength absorption measurements: Method
931 and application to AERONET and Aethalometer observations, *Atmos. Chem. Phys.*, 16(19), 12733–12752,
932 doi:10.5194/acp-16-12733-2016, 2016.

933 Wang, X., Heald, C. L., Liu, J., Weber, R. J., Campuzano-Jost, P., Jimenez, J. L., Schwarz, J. P. and Perring, A. E.:
934 Exploring the observational constraints on the simulation of brown carbon, *Atmos. Chem. Phys.*, 18(2), 635–653,
935 doi:10.5194/acp-18-635-2018, 2018.

936 Wei, Y., Ma, L., Cao, T., Zhang, Q., Wu, J., Buseck, P. R. and Thompson, J. E.: Light scattering and extinction
937 measurements combined with laser-induced incandescence for the real-time determination of soot mass absorption
938 cross section, *Anal. Chem.*, 85(19), 9181–9188, doi:10.1021/ac401901b, 2013.

939 Westerling, A. L., Hidalgo, H. G., Cayan, D. R. and Swetnam, T. W.: Warming and Earlier Spring Increase Western
940 U. S. Forest Wildfire Activity, *Science*, 313(5789), 940–943, doi:10.1126/science.1128834, 2006.

941 Williams, E. L. and Grosjean, D.: Removal of Atmospheric Oxidants with Annular Denuders, *Environ. Sci. Technol.*,
942 24(6), 811–814, doi:10.1021/es00076a002, 1990.

943 Wonaschütz, A., Hitzenberger, R., Bauer, H., Pournesmaeil, P., Klatzer, B., Caseiro, A. and Puxbaum, H.: Application
944 of the integrating sphere method to separate the contributions of brown and black carbon in atmospheric aerosols,
945 *Environ. Sci. Technol.*, 43(4), 1141–1146, doi:10.1021/es8008503, 2009.

946 Yue, X., Mickley, L. J., Logan, J. A. and Kaplan, J. O.: Ensemble projections of wildfire activity and carbonaceous
947 aerosol concentrations over the western United States in the mid-21st century, *Atmos. Environ.*, 77, 767–780,
948 doi:10.1016/j.atmosenv.2013.06.003, 2013.

949 Zeng, L., Zhang, A., Wang, Y., Wagner, N. L., Katich, J. M., Schwarz, J. P., Schill, G. P., Brock, C., Froyd, K. D.,
950 Murphy, D. M., Williamson, C. J., Kupc, A., Scheuer, E., Dibb, J. and Weber, R. J.: Global Measurements of Brown
951 Carbon and Estimated Direct Radiative Effects, *Geophys. Res. Lett.*, 47(13), doi:10.1029/2020GL088747, 2020.

952 Zeng, L., Sullivan, A. P., Washenfelder, R. A., Dibb, J., Scheuer, E., Campos, T. L., Katich, J. M., Levin, E., Robinson,
953 M. A. and Weber, R. J.: Assessment of online water-soluble brown carbon measuring systems for aircraft sampling,
954 *Atmos. Meas. Tech.*, 14(10), 6357–6378, doi:10.5194/amt-14-6357-2021, 2021.

955 Zeng, L., Dibb, J., Scheuer, E., Katich, J. M., Schwarz, J. P., Bourgeois, I., Peischl, J., Ryerson, T., Warneke, C.,
956 Perring, A. E., Diskin, G. S., Digangi, J. P., Nowak, J. B., Moore, R. H., Wiggins, E. B., Pagonis, D., Guo, H.,
957 Campuzano-jost, P., Jimenez, J. L., Xu, L. and Weber, R. J.: Characteristics and Evolution of Brown Carbon in
958 Western United States Wildfires, *Atmos. Chem. Phys.*, 22, 8009–8036, doi:10.5194/acp-22-8009-2022, 2022.

959 Zhang, L., Segal-Rozenhaimer, M., Che, H., Dang, C., Sedlacek, A. J., Lewis, E. R., Dobracki, A., Wong, J. P. S.,
960 Formenti, P., Howell, S. G. and Nenes, A.: Light absorption by brown carbon over the South-East Atlantic Ocean,
961 *Atmos. Chem. Phys.*, 22(14), 9199–9213, doi:10.5194/acp-22-9199-2022, 2022.

962 Zhang, Y., Forrister, H., Liu, J., Dibb, J., Anderson, B., Schwarz, J. P., Perring, A. E., Jimenez, J. L., Campuzano-Jost,
963 P., Wang, Y., Nenes, A. and Weber, R. J.: Top-of-atmosphere radiative forcing affected by brown carbon in the
964 upper troposphere, *Nat. Geosci.*, 10(7), 486–489, doi:10.1038/ngeo2960, 2017.

965